JEM Journal of Experimental Medicine

ARTICLE

Stearoyl-CoA desaturase-1 impairs the reparative properties of macrophages and microglia in the brain

Jeroen F.J. Bogie[1*], Elien Grajchen[1*], Elien Wouters[1], Aida Garcia Corrales[1], Tess Dierckx[1], Sam Vanherle[1], Jo Mailleux[1], Pascal Gervois[2], Esther Wolfs[2], Jonas Dehairs[3], Jana Van Broeckhoven[1], Andrew P. Bowman[4], Ivo Lambrichts[2], Jan-Åke Gustafsson[5,6], Alan T. Remaley[7], Monique Mulder[8], Johannes V. Swinnen[3], Mansour Haidar[1], Shane R. Ellis[4], James M. Ntambi[9,10], Noam Zelcer[11], and Jerome J.A. Hendriks[1]

Failure of remyelination underlies the progressive nature of demyelinating diseases such as multiple sclerosis. Macrophages and microglia are crucially involved in the formation and repair of demyelinated lesions. Here we show that myelin uptake temporarily skewed these phagocytes toward a disease-resolving phenotype, while sustained intracellular accumulation of myelin induced a lesion-promoting phenotype. This phenotypic shift was controlled by stearoyl-CoA desaturase-1 (SCD1), an enzyme responsible for the desaturation of saturated fatty acids. Monounsaturated fatty acids generated by SCD1 reduced the surface abundance of the cholesterol efflux transporter ABCA1, which in turn promoted lipid accumulation and induced an inflammatory phagocyte phenotype. Pharmacological inhibition or phagocyte-specific deficiency of *Scd1* accelerated remyelination ex vivo and in vivo. These findings identify SCD1 as a novel therapeutic target to promote remyelination.

Introduction

A major pathological hallmark of neuroinflammatory disorders such as multiple sclerosis (MS) is the accumulation of peripherally derived macrophages and resident microglia within the central nervous system (CNS; Ajami et al., 2011; Bogie et al., 2014; Mildner et al., 2009). Until recently, these phagocytes were mainly thought to boost lesion progression. Disease-promoting effector functions include the release of inflammatory and toxic mediators that negatively impact neuronal and oligodendrocyte integrity (Nikić et al., 2011; Trapp et al., 1998), internalization of the intact myelin sheath (Yamasaki et al., 2014), and the presentation of CNS-derived antigens to autoreactive T cells (McMahon et al., 2005). However, this notion has been challenged in recent years, and it is now clear that phagocytes also have disease-resolving functions in neurological disorders (Grajchen et al., 2018). For example, clearance of damaged myelin is essential to facilitate CNS repair (Miron et al., 2013; Ruckh et al., 2012). Moreover, ingestion of myelin by phagocytes reshapes their phenotype to one that is typically associated with wound healing and is accompanied by reduced expression of inflammatory mediators (Bogie et al., 2011; Boven et al., 2006; Hikawa and Takenaka, 1996). We recently found that this protective phenotype is closely linked to the activation of lipid-responsive signaling pathways, such as the liver X receptor (LXR) and peroxisome proliferator-activated receptor signaling pathways (Bogie et al., 2012, 2013). At the same time, a number of studies indicate that myelin-containing foam cells also display inflammatory features (van der Laan et al., 1996; Wang et al., 2015; Williams et al., 1994). To date, it remains unclear which signals direct foam cells in the CNS to acquire a disease-promoting or -resolving phenotype. Identifying the molecular pathways that direct the phenotype of foamy phagocytes in the CNS is essential for our understanding of lesion progression in neurodegenerative disorders and for the development of reparative therapies.

Here, we report that sustained intracellular accumulation of myelin counteracts the reparative phenotype of phagocytes in demyelinating disorders. This phenotypic shift is orchestrated by stearoyl-CoA desaturase-1 (SCD1), an enzyme that catalyzes

[1]Department of Immunology and Infection, Biomedical Research Institute, Hasselt University, Diepenbeek, Belgium; [2]Department of Cardio and Organ Systems, Biomedical Research Institute, Hasselt University, Diepenbeek, Belgium; [3]Department of Oncology, Laboratory of Lipid Metabolism and Cancer, Leuven Cancer Institute, University of Leuven, Leuven, Belgium; [4]The Maastricht MultiModal Molecular Imaging Institute, Division of Imaging Mass Spectrometry, Maastricht University, Maastricht, Netherlands; [5]Center for Nuclear Receptors and Cell Signaling, University of Houston, Houston, TX; [6]Department of Biosciences and Nutrition, Karolinska Institutet, Huddinge, Sweden; [7]Lipoprotein Metabolism Laboratory, Translational Vascular Medicine Branch, National Heart, Lung, and Blood Institute, National Institutes of Health, Bethesda, MD; [8]Department of Internal Medicine, Erasmus University Medical Center, Rotterdam, Netherlands; [9]Department of Biochemistry, University of Wisconsin-Madison, Madison, WI; [10]Department of Nutritional Sciences, University of Wisconsin-Madison, Madison, WI; [11]Department of Medical Biochemistry, Academic Medical Center, University of Amsterdam, Amsterdam, Netherlands.

*J.F.J. Bogie and E. Grajchen contributed equally to this paper; Correspondence to Jerome J.A. Hendriks: Jerome.hendriks@uhasselt.be; Jeroen F.J. Bogie: Jeroen.bogie@uhasselt.be.

the rate-limiting step in the conversion of saturated (SFA) into mono-unsaturated fatty acids (MUFAs). We show that SCD1-derived MUFAs induce inflammatory foam cell formation by impairing ABCA1-mediated cholesterol efflux. Depletion of SCD1 in phagocytes prevents the myelin-induced phenotype shift and promotes remyelination. Our findings highlight the importance of fatty acid (FA) desaturation in controlling foamy phagocyte function in MS and potentially other neurodegenerative disorders.

Results

Myelin overload skews phagocytes toward an inflammatory phenotype

Phagocytes are the most abundant immune cells in active MS lesions, and the majority of them show intracellular myelin remnants (Grajchen et al., 2018). As cholesterol is a major constituent of myelin, it represents an ideal parameter to define the intracellular myelin load within foamy phagocytes. Accordingly, by visualizing myelin-derived cholesterol, we found increased free cholesterol (FC; filipin staining) and esterified cholesterol (EC; Oil Red O [ORO] staining) in myelin-containing phagocytes (mye-phagocytes) in active lesions in postmortem brain tissue of MS patients (Fig. 1, A–D). In line with lesion expansion, actively phagocytosing cells in the rim of MS lesions showed a lower cholesterol burden as compared with those in the lesion center that have accumulated myelin for a longer period of time (Fig. 1, A–D). Phagocytes in the normal-appearing white matter (NAWM) of MS patients and non-neurological controls showed no cholesterol accumulation (Fig. 1, A–D; and Fig. S1, A and B).

Given the controversy around the phenotype of mye-phagocytes (Grajchen et al., 2018), we next determined the impact of the intracellular myelin load on the inflammatory phenotype of phagocytes. For this purpose, mouse bone marrow–derived macrophages (BMDMs), mouse microglia, and human monocyte-derived macrophages (MDMs) were treated for 24 or 72 h with myelin (mye^{24}- or mye^{72}-BMDMs/microglia/MDMs; experimental design in Fig. S1 C). To validate the intracellular accumulation of myelin, we first assessed the cholesterol content of mye^{24}- and mye^{72}-phagocytes. Prolonged incubation with myelin markedly increased the presence of total cholesterol, FC, and EC in all phagocyte subsets (Fig. 1, E–G). Given that in the lesion environment macrophages and microglia are exposed to inflammatory mediators, the phenotype of mye-phagocytes was defined following stimulation with the prototypical inflammatory stimulus LPS and disease-relevant inflammatory cytokines IFN-G and IL-1B. Interestingly, in parallel to increasing the intracellular cholesterol load, prolonged uptake of myelin countered the initial less inflammatory phenotype of mye-phagocytes upon stimulation with LPS (Fig. 2, A–C), while not influencing cell viability (Fig. S1 D). Likewise, while short-term incubation with myelin induced a less-inflammatory phenotype of IFN-G/IL-1B–stimulated MDMs, BMDMs, and microglia, prolonged incubation with myelin skewed these cells toward a more inflammatory phenotype (Fig. S1 E). Moreover, akin to the in vitro experiments, myelin load closely correlated with the phenotype of phagocytes within active lesions in postmortem brain tissue of MS patients. Foamy phagocytes in the lesion center, containing abundant intracellular myelin remnants (Fig. 1, A–D), showed a more pronounced immunoreactivity for the inflammatory markers CCR7 (Van Raemdonck et al., 2019), CD32 (Kigerl et al., 2009), and IL-1B compared with foamy phagocytes in the lesion rim that contained less intracellular myelin (Fig. 2, D–I). Also, the density of phagocytes expressing CCR7, CD32, and IL-1B was increased in the lesion center compared with the lesion rim (Fig. 2, J–L). Collectively, these findings indicate that sustained accumulation of myelin skews macrophages and microglia toward an inflammatory phenotype.

SCD1 drives the inflammatory phenotype shift of foamy phagocytes

Our previously reported transcriptomic analysis identified *Scd1*, the rate-limiting enzyme in the conversion of SFA into MUFAs, as one of the most potently induced genes in macrophages after prolonged uptake of myelin (Bogie et al., 2012). SCD1 belongs to the family of Δ9-FA desaturases (mouse; SCD1-4, human; SCD1 and 5), which exhibit different tissue and cell distribution patterns (Flowers and Ntambi, 2008). Here, we found that myelin exposure robustly increased the mRNA expression of *Scd1* but not of the other *Scd* isoforms in BMDMs, and to a lesser extent also in microglia and MDMs (Fig. 3 A). This increase in *Scd1* mRNA was accompanied by a higher SCD1 protein level (Fig. 3 B and Fig. S1 F). In particular, cells with high granularity (side scatter [SSC]^{hi}), corresponding to cells that internalized large amounts of myelin, showed the highest level of SCD1 (Fig. 3 B). Previous studies demonstrated that SCD1 is a transcriptional target of LXRs through SREBP1C (Chu et al., 2006; Zhang et al., 2014). In line with this, we find that LXRβ, and not LXRα, was the predominant isoform to control SCD1 protein level in BMDMs upon myelin exposure (Fig. S1 G).

To determine the desaturation level of FAs in mye-phagocytes, a proxy for SCD1 activity, electrospray ionization tandem mass spectrometry (ESI-MS/MS) analysis was performed. Sustained accumulation of myelin in BMDMs reduced the level of SFAs and increased that of unsaturated FAs (UFAs) in intact phosphatidylcholine (PC; Fig. 3 C), which is the most abundant phospholipid family in mammalian membranes. This finding suggests that SCD1 activity is increased in phagocytes after prolonged uptake of myelin. In support of this notion, gas chromatography mass spectrometry (GC-MS) analysis of hydrolyzed FAs derived from mye^{72}-BMDMs showed increased 16:1/16:0 and 18:1/18:0 desaturation indices compared with control cells (Fig. 3 D). Collectively, our findings show that myelin internalization increases SCD1 abundance and activity in phagocytes.

Given that foamy phagocytes are abundant in active lesions of MS patients, we next determined whether myelin internalization also increased the level and activity of SCD1 in phagocytes in these lesions. Fluorescent double staining demonstrated that the majority of IBA1$^+$ phagocytes in the rim and center of active MS lesions expressed SCD1 and that SCD1 was primarily expressed by IBA1$^+$ phagocytes (Fig. 3, E and F; and Fig. S1, H and I). A gradual increase of SCD1 intensity in IBA1$^+$ cells was observed toward the lesion center (Fig. 3 E). As phagocytes in the lesion center have a higher cholesterol load compared with those in the lesion rim, this finding suggests an association between

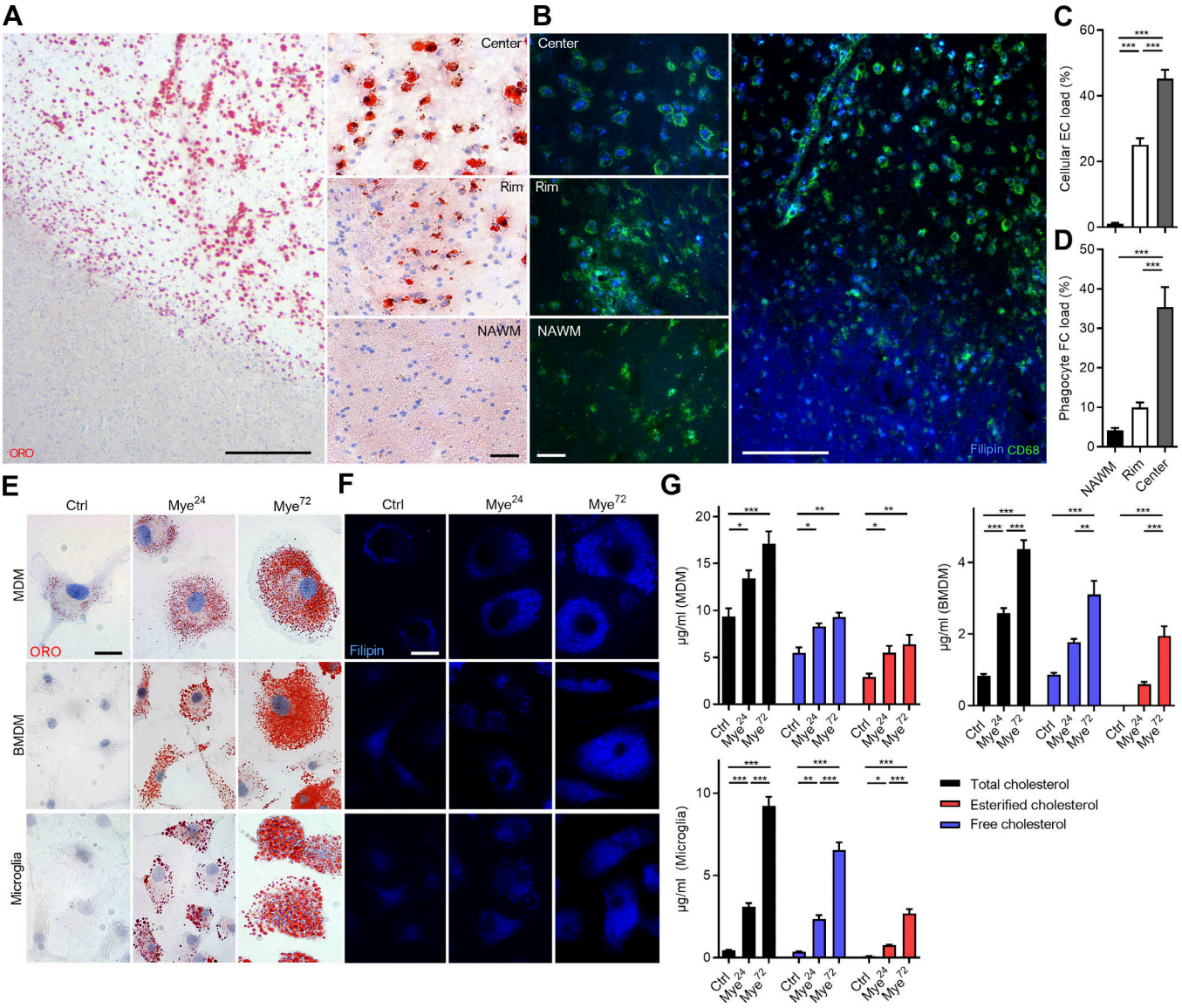

Figure 1. **Sustained exposure to myelin increases the intracellular cholesterol load in phagocytes. (A–D)** Representative images and quantification of ORO (EC) and filipin (FC) staining of active lesion in postmortem brain tissue of MS patients (n = 3 lesions from three different MS patients). Phagocyte EC and FC load was determined by defining the cellular area covered by ORO$^+$ and FC$^+$ droplets. Scale bars, 500 µm (overview); 50 µm (inset). **(E and F)** Representative images of ORO and filipin staining of mouse BMDMs, mouse microglia, and human MDMs treated with myelin for 24 or 72 h, or left untreated (Ctrl). Scale bar, 30 µm. **(G)** Quantification of total cholesterol, FC, and EC in BMDMs (n = 7 wells), microglia (n = 5 wells), and MDMs (n = 7 wells) treated with myelin for 24 or 72 h, or left untreated (Ctrl). Results are pooled from or representative of two (E–G) or three (A–D) independent experiments. Human MDM cultures from seven donors were used (G). All data are represented as mean ± SEM. *, P < 0.05, **, P < 0.01, and ***, P < 0.001, one-way ANOVA.

sustained intracellular accumulation of myelin and SCD1 abundance in active MS lesions. To define whether elevated SCD1 protein level was associated with increased SFA desaturation, MUFA-containing PC lipid species were visualized in active MS lesions using matrix-assisted laser/desorption ionization-mass spectrometry imaging. We found an increased PC 36:2/PC 36:1 ratio in lesions compared with adjacent NAWM (Fig. 3 G; individual ion images and second active MS lesion are shown in Fig. S1, J–L). Tandem mass spectrometry analysis confirmed the PC 36:2 lipid species to consist primarily of two MUFA 18:1 fatty acyl chains. As active SCD1 signaling results in the formation of 18:1 fatty acyl chains, these findings are consistent with increased desaturase activity within active lesions of MS patients.

As our data show that SCD1 expression coincides with an increased inflammatory phenotype of phagocytes after prolonged uptake of myelin, we next determined if SCD1 is involved in directing this phenotype. To test this, an SCD1-selective inhibitor was used (CAY10566; Chen et al., 2016). Consistent with SCD1 inhibition, mye-BMDMs exposed to the SCD1 inhibitor showed an increase in SFAs and a decrease in UFAs (Fig. S2 A). Importantly, SCD1 inhibition prevented the inflammatory phenotypic shift associated with prolonged myelin uptake (Fig. 4 A), and attenuated release of NO and TNF-A by mye^{72}-BMDMs (Fig. 4 B). An identical phenotype shift was observed using BMDMs isolated from *Scd1*$^{-/-}$ mice (Fig. 4, A and B). Similar to BMDMs, microglia and MDMs treated with the SCD1 inhibitor

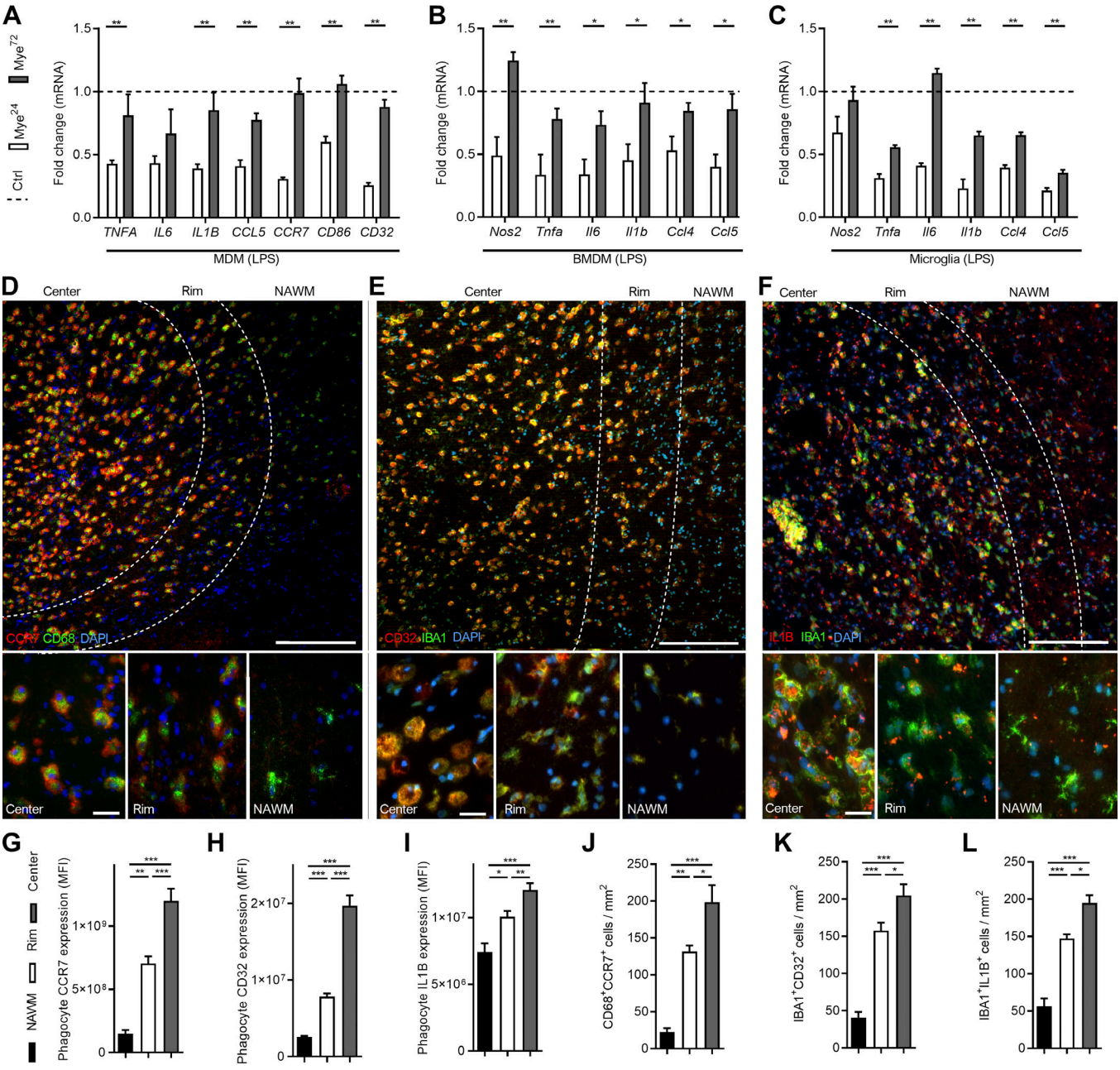

Figure 2. **Prolonged exposure to myelin promotes an inflammatory phagocyte phenotype. (A–C)** mRNA expression of inflammatory factors in LPS-stimulated human MDMs (n = 7 wells), mouse BMDMs (n = 5 wells), and mouse microglia (n = 6 wells) treated with myelin for 24 or 72 h, or left untreated (dotted line, Ctrl). **(D–L)** Representative immunofluorescence images and quantification (MFI of CCR7, CD32, and IL-1B in phagocytes, and number of phagocytes expressing CCR7, CD32, and IL-1B) of an active MS lesion stained with CCR7/CD68, CD32/IBA1, and IL-1B/IBA1 (n = 3 lesions from three different MS patients). Scale bars, 500 µm (overview); 50 µm (inset). Results are pooled from or representative of two (B and C) or three (D–L) independent experiments. Human MDM cultures from seven donors were used (A). All data are represented as mean ± SEM. *, P < 0.05, **, P < 0.01, and ***, P < 0.001, unpaired Student's t test (A–C), one-way ANOVA (G–L).

showed a decreased inflammatory response upon prolonged myelin exposure (Fig. 4, C and D). Notably, inhibition of SCD1 activity did not impact the expression of neurotrophic factors in all mye-phagocyte subsets (Fig. S2 B). These findings position SCD1 as an important mediator of the inflammatory status of myelin-phagocytosing macrophages and microglia.

Parallel to reducing the inflammatory status of mye-phagocytes, SCD1 inhibition or genetic deficiency lowered intracellular cholesterol load in all phagocyte subsets after prolonged myelin uptake (Fig. 4, E and F), a reduction that was not a result of reduced viability or decreased phagocytic capacity (Fig. S2, C and D). Transmission electron microscopy further demonstrated that inhibition of SCD1 reduced the number of lipid droplets within mye^{72}-BMDMs without affecting their size (Fig. S2, E–G). In contrast, myelin-containing organelles, comprising lysosomes and endosomes, were significantly reduced in size in

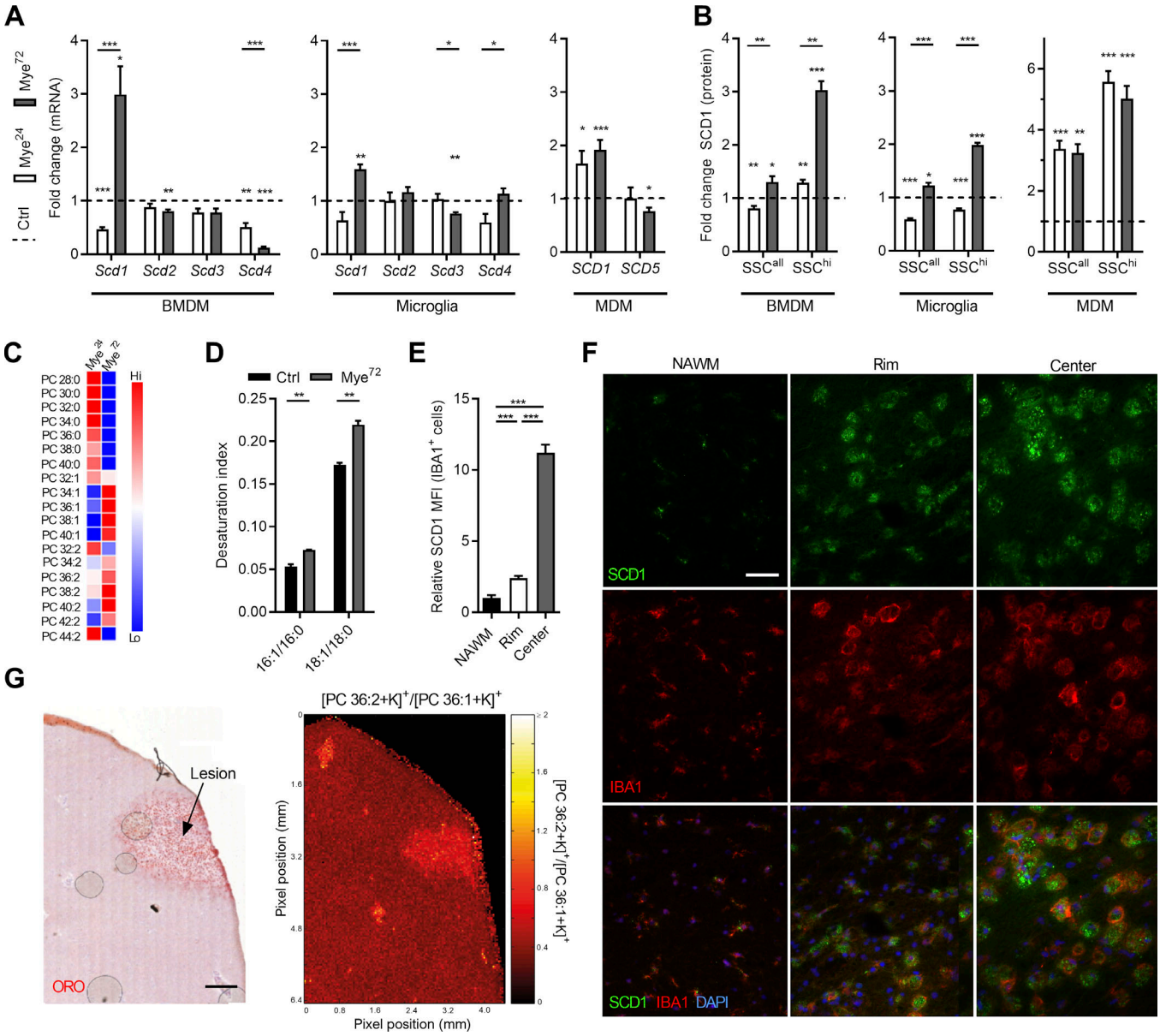

Figure 3. **Myelin internalization increases SCD1 abundance and activity in phagocytes. (A)** mRNA expression of *Scd* isoforms in myelin-treated BMDMs, microglia, and MDMs (24 and 72 h, $n = 6$ wells). Dotted line represents untreated cells (Ctrl). **(B)** Flow-cytometric analysis of SCD1 abundance in myelin-treated BMDMs, microglia, and MDMs (24 and 72 h, $n = 6$ wells). Side scatter measurement was used to identify phagocytes that internalized little (SSC^{lo}) and large (SSC^{hi}) amounts of myelin. Dotted line represents untreated cells (Ctrl). **(C)** ESI-MS/MS–based lipidomics analysis of intact PC in myelin-treated BMDMs (24 and 72 h, $n = 2$ wells). **(D)** GC/MS analysis of the methyl esters of FAs hydrolyzed from untreated and myelin-treated BMDMs (72 h). Desaturation indices were determined by calculating the 16:1/16:0 and 18:1/18:0 ratios ($n = 4$ wells). **(E and F)** Representative images and quantification (MFI) of SCD1 in lesional phagocytes. Active MS lesions were stained for SCD1/IBA1 ($n = 3$ lesions from three different MS patients). Scale bar, 50 µm. **(G)** Mass spectrometry image of the ratio of intact PC lipid species and corresponding ORO staining of an active MS lesion. The PC 36:2/PC 36:1 ratio was calculated based on intensity images of individual PC lipid species (Fig. S1 J). A second active MS lesion is shown in Fig. S1, K and L. Scale bar, 500 µm. Results are pooled from or representative of two (A–D and G) or three (E and F) independent experiments. Human MDM cultures from six donors were used (A). All data are represented as mean ± SEM. *, $P < 0.05$, **, $P < 0.01$, and ***, $P < 0.001$, unpaired Student's *t* test (A, B, and D), one-way ANOVA (E).

mye^{72}-BMDMs treated with the SCD1 inhibitor (Fig. S2, E–G). These findings show that SCD1 inhibition promotes the processing and potential clearance of myelin by phagocytes.

SCD1-derived FAs reduce ABCA1 surface abundance through protein kinase C δ (PKCδ)

The above results indicate that SCD1 deficiency reduces intracellular cholesterol levels in mye-phagocytes without affecting their phagocytic capacity. Given the importance of lipid efflux in controlling cellular cholesterol load, we next determined the expression and activity of the cholesterol efflux transporter ABCA1. Myelin uptake increased the mRNA expression of *Abca1* in BMDMs, microglia, and MDMs, with mye^{72}-phagocytes showing the highest expression (Fig. 5 A). Counterintuitively, while short-term treatment with myelin increased surface abundance of ABCA1, mye^{72}-BMDMs and -microglia had reduced

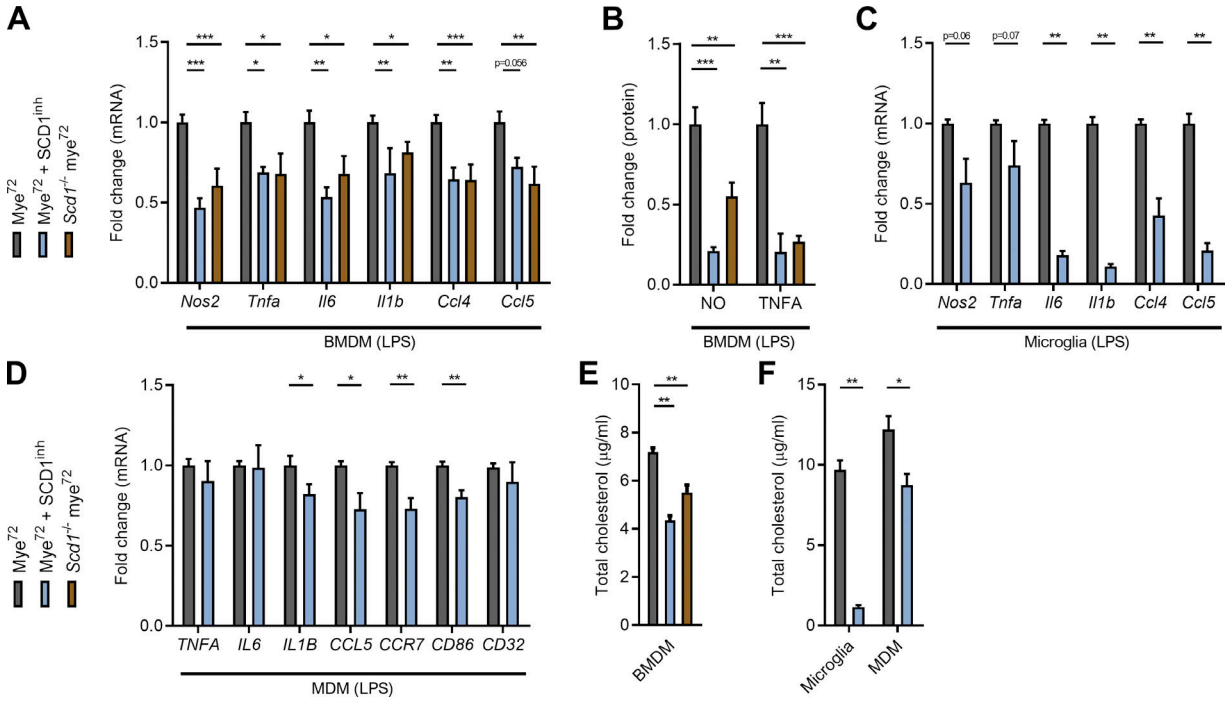

Figure 4. **SCD1 controls the inflammatory phenotype shift of mye-phagocytes. (A)** mRNA expression of inflammatory mediators in LPS-stimulated WT, *Scd1*$^{-/-}$, and SCD1 inhibitor-treated BMDMs exposed to myelin for 72 h (n = 5 wells). **(B)** NO and TNF-A concentration in culture supernatants of LPS-stimulated WT, *Scd1*$^{-/-}$, and SCD1 inhibitor-treated mye^{72}-BMDMs (n = 5 wells). **(C and D)** mRNA expression of inflammatory mediators in LPS-stimulated mouse microglia (n = 6 wells) and human MDMs (n = 8 wells) exposed to myelin and an SCD1 inhibitor for 72 h. **(E and F)** Quantification of total cholesterol in WT, *Scd1*$^{-/-}$, and SCD1 inhibitor-treated mye^{72}-BMDMs (E, n = 6 wells), and SCD1-inhibitor treated mye^{72}-microglia (F, n = 6 wells) and -MDMs (F, n = 8 wells). Results are pooled from two independent experiments (A–C, E, and F). Human MDM cultures from four donors were used (D and F). All data are represented as mean ± SEM. *, P < 0.05, **, P < 0.01, and ***, P < 0.001, one-way ANOVA (A, B, and E), unpaired Student's t test (C, D, and F).

surface levels of ABCA1 (Fig. 5, B and C). MDMs showed a trend toward decreased surface ABCA1 levels after prolonged myelin uptake (Fig. 5 D). Interestingly, SCD1 inhibition and genetic deficiency prevented the reduction in surface ABCA1 levels on all mye^{72}-phagocyte subsets (Fig. 5, B–D). A similar reduction in ABCA1 levels upon prolonged exposure to myelin was observed in HeLa cells expressing a functional human ABCA1-GFP fusion protein (HeLa-ABCA1^{gfp}, Fig. S3 A). HeLa cells efficiently internalized and processed myelin (Fig. S3, B–D). Consistent with surface ABCA1 levels, cholesterol efflux toward the ABCA1-dependent lipid acceptor apoA-I was attenuated in mye^{72}-phagocytes in an SCD1-dependent manner (Fig. 5, E–G). To identify which FAs are responsible for impaired ABCA1-mediated cholesterol efflux, the FA profile of mye-BMDMs was measured. Myelin accumulation not only increased intracellular levels of palmitoleic acid (16:1) and oleic acid (18:1), in line with elevated SCD1 activity, but also markedly increased gondoic acid (20:1) and nervonic acid (24:1; Fig. S3, E and F). The latter finding indicates active elongation of SCD1-derived FAs. By using HeLa-ABCA1^{gfp} cells, we further show that palmitoleic, oleic, gondoic, and erucic acid (22:1) reduced total ABCA1 abundance upon internalization (Fig. S3, G and H). To test whether accumulation of these FA species reduces ABCA1-mediated cholesterol efflux, BMDMs were treated with each of the aforementioned FAs. We found that oleic, gondoic, and nervonic acid reduced ABCA1-mediated cholesterol efflux, while palmitoleic acid and erucic acid did not have an effect (Fig. 5 H). In summary, these findings indicate that SCD1-derived MUFAs reduce the capacity of mye-phagocytes to efflux cholesterol via ABCA1.

Interestingly, analysis of human postmortem brain tissue demonstrated that surface ABCA1 abundance also inversely correlated with SCD1 protein level and intracellular lipid load within phagocytes in MS lesions. Whereas phagocytes in the lesion rim displayed a clear surface ABCA1 staining pattern, phagocytes in the lesion center showed a predominant intracellular localization of ABCA1, as well as an overall reduced level of ABCA1 (Fig. 5, I–L). This ABCA1 expression pattern closely corresponds to the abundant presence of cholesterol and increased magnitude of SCD1 expression within phagocytes in the lesion center compared with the lesion rim (Fig. 1, A–D; and Fig. 3, E and F).

The discrepancy between ABCA1 mRNA and protein levels in our in vitro experiments suggests that post-transcriptional modifications underlie the loss of surface ABCA1 abundance on phagocytes after prolonged exposure to myelin (Fig. 5, A–D). As MUFAs are reported to decrease ABCA1 abundance on the cell surface in a PKCδ-dependent manner (Sun et al., 2003; Wang and Oram, 2002, 2007; Yang et al., 2010), we reasoned that PKCδ might control ABCA1 surface level, cholesterol load, and the phenotype of mye-phagocytes as well. By using the PKCδ inhibitor rottlerin (Gschwendt et al., 1994), we show that inhibition of PKCδ increased surface abundance of ABCA1 on

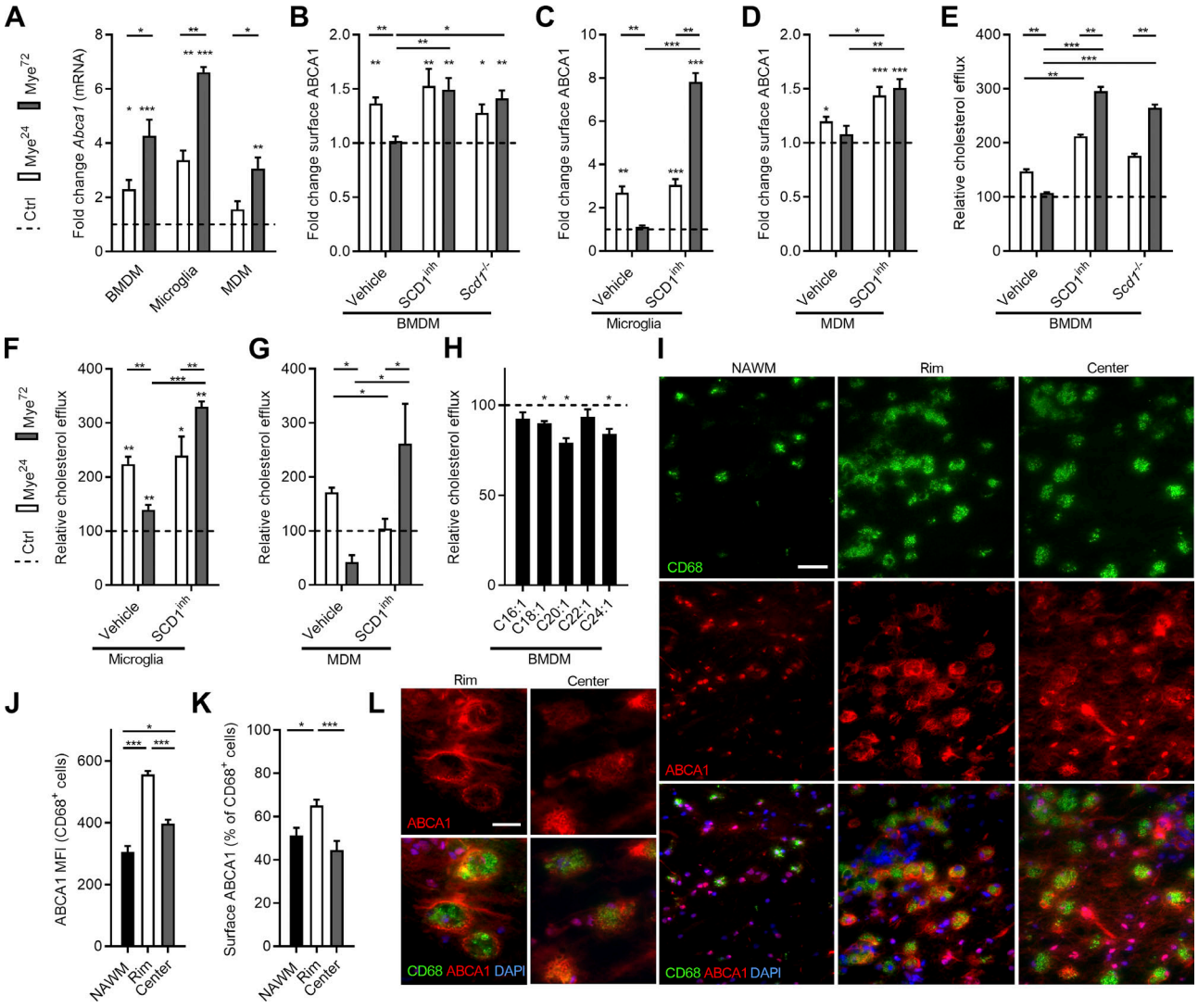

Figure 5. **Myelin uptake decreases ABCA1 surface levels in an SCD1-dependent manner. (A)** mRNA expression of *Abca1* in BMDMs (n = 5 wells), microglia (n = 6 wells), and MDMs (n = 6 wells) treated with myelin for 24 and 72 h. Dotted line represents untreated cells (Ctrl). **(B–G)** Surface ABCA1 abundance (n = 5 or 6 wells) and relative capacity to efflux cholesterol (n = 6 wells) of WT, *Scd1*$^{-/-}$, and SCD1 inhibitor-treated BMDMs exposed to myelin for 24 or 72 h (B and E), and mye-microglia (C and F) and mye–MDM (D and G) treated with the SCD1 inhibitor. Dotted line represents untreated cells (Ctrl). **(H)** Cholesterol efflux capacity of BMDMs treated with different MUFAs (50 µM; n = 3 wells). **(I–L)** Representative immunofluorescence images and quantification (MFI of ABCA1 in phagocytes and percentage of phagocytes expressing ABCA1 on the cell surface within the phagocyte pool) of an active MS lesion stained for ABCA1/CD68 (n = 3 lesions from three different MS patients). Scale bars, 50 µm (I); 20 µm (L). Results are pooled from or representative of two (A–H) or three (I–L) independent experiments. Human MDM cultures from six donors were used (A, D, and G). All data are represented as mean ± SEM. *, P < 0.05, **, P < 0.01, and ***, P < 0.001, unpaired Student's t test (A and H), one-way ANOVA (B–G, J, and K).

mye^{72}-phagocytes but not mye^{24}-phagocytes (Fig. 6 A and Fig. S3 I). Elevated ABCA1 surface levels on mye^{72}-phagocytes were accompanied by a reduction in cellular cholesterol load (Fig. 6, B–E) and a decreased expression of inflammatory mediators (Fig. 6, F–H). Collectively, these findings provide evidence that PKCδ controls lipid efflux and the inflammatory status of mye^{72}-phagocytes.

SCD1-mediated loss of ABCA1 leads to the accumulation of inflammatory FC

Loss of ABCA1 drives phagocytes toward an inflammatory phenotype by promoting the accumulation of inflammatory FC (Tall and Yvan-Charvet, 2015; Yvan-Charvet et al., 2008). By using *Abca1*$^{-/-}$ BMDMs (Fig. S3, J and K), we found that loss of ABCA1 also accelerated the accumulation of FC in mye-BMDMs (Fig. 7 A). Given that prolonged exposure to myelin significantly reduced the viability of *Abca1*$^{-/-}$ BMDMs (Fig. S3 L), subsequent experiments were performed using *Abca1*$^{-/-}$ mye^{24}-BMDMs. Interestingly, *Abca1*$^{-/-}$ BMDMs acquired an inflammatory phenotype already upon short-term incubation with myelin (mye^{24}-BMDMs; Fig. 7 B). To establish a causal link between SCD1, ABCA1, and the inflammatory phenotype of mye-BMDMs, *Abca1*$^{-/-}$ mye^{24}-BMDMs were treated with the SCD1 inhibitor. In the absence of ABCA1, inhibition of SCD1 did not attenuate the inflammatory phenotype of mye^{24}-BMDMs, nor did it decrease the intracellular FC load (Fig. 7, C and D). These results

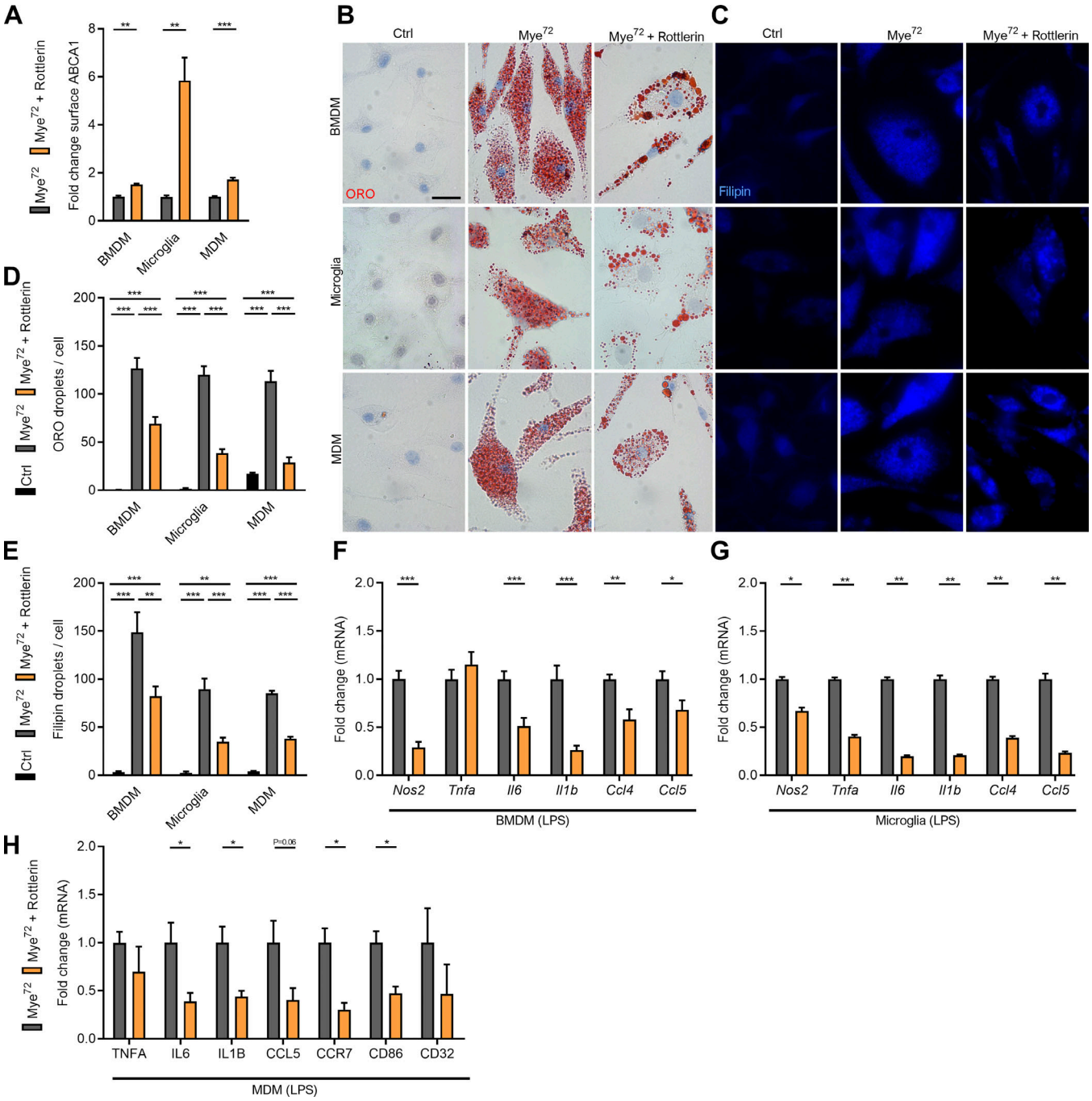

Figure 6. **Myelin uptake impacts the metabolic and inflammatory phenotype of phagocytes in a PKCδ-dependent manner. (A)** Surface ABCA1 abundance on myelin-treated mouse BMDMs (n = 5 wells), mouse microglia (n = 6 wells), and human MDMs (n = 4 wells) exposed to rottlerin (PKCδ inhibitor) or vehicle**. (B–E)** Representative images and quantification of ORO (EC) and filipin (FC) staining of untreated phagocytes (Ctrl) and mye^{72}-phagocytes treated with rottlerin or vehicle (n = 4 wells). Scale bar, 20 µm. **(F–H)** mRNA expression of inflammatory mediators in LPS-stimulated mye^{72}-BMDMs (n = 11 wells), -microglia (n = 6), and -MDMs (n = 4 wells) treated with rottlerin or vehicle. Results are pooled from or representative of two (A–E, G, and H) or three (F) independent experiments. Human MDM cultures from four donors were used (A–E and H). All data are represented as mean ± SEM. *, P < 0.05, **, P < 0.01, and ***, P < 0.001, unpaired Student's t test (A, F, G, and H), one-way ANOVA (D and E).

suggest that SCD1 skews mye-phagocytes toward an inflammatory phenotype by reducing ABCA1 surface levels and efflux capacity. In addition, they suggest that accumulation of FC due to a decrease in ABCA1 underlies the induction of this inflammatory phenotype in mye^{72}-phagocytes. To test this, mye^{72}-phagocytes were depleted of FC using methyl-β-cyclodextrin (MβCD). MβCD (2.5% m/v) efficiently removed FC without affecting the level of EC and cell viability (Fig. S3, M and N). Importantly, MβCD reduced the inflammatory phenotype of *Abca1*$^{-/-}$ mye^{24}-BMDMs and all mye^{72}-phagocyte subsets (Fig. 7, E–H). The latter experiments demonstrate that removal of FC is sufficient to block the induction of an inflammatory phenotype

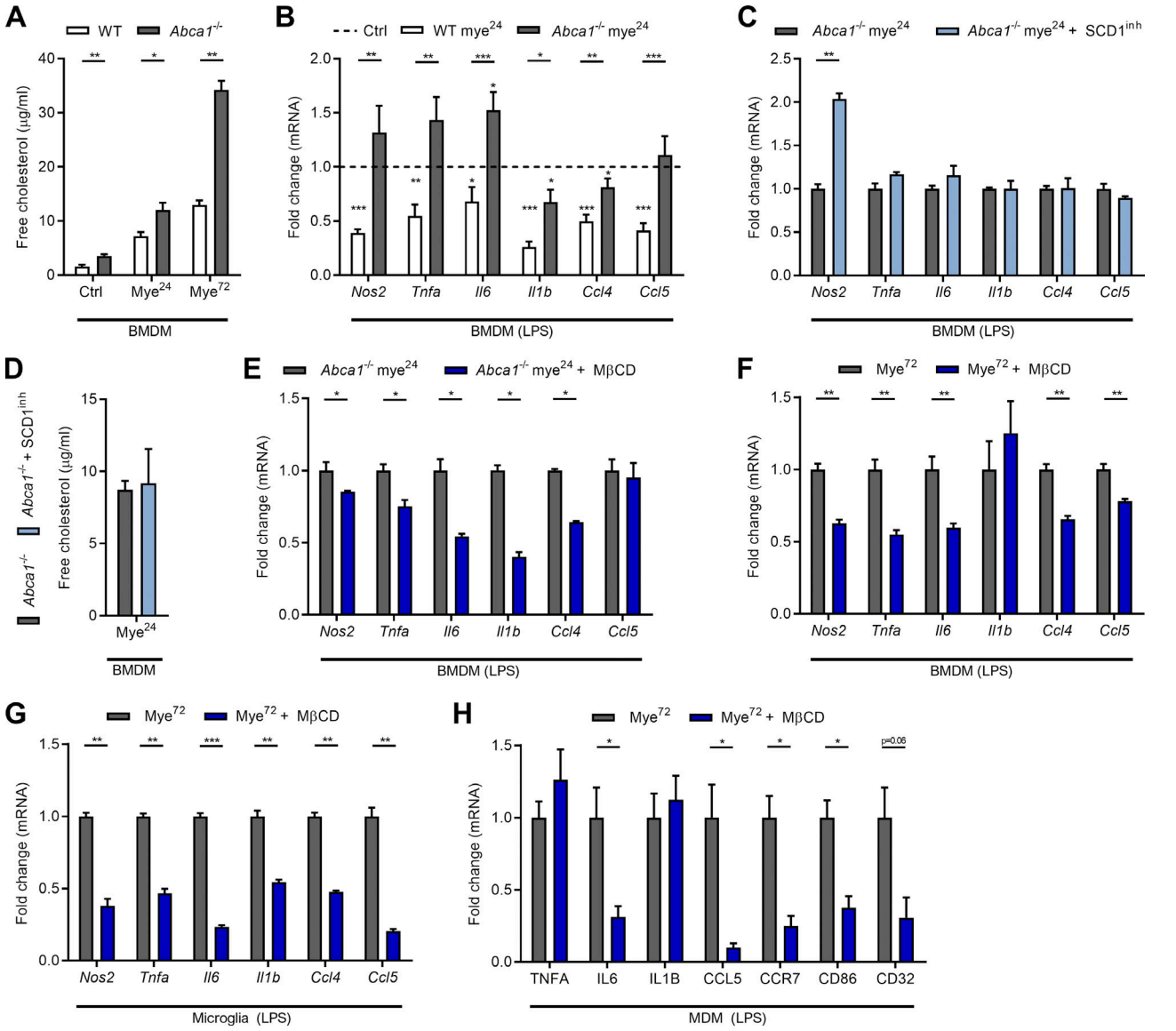

Figure 7. **Accumulation of inflammatory FC underlies the SCD1-induced phenotype shift. (A)** Quantification of FC in WT and *Abca1*$^{-/-}$ BMDMs treated with myelin for 24 or 72 h (mye^{24}- or mye^{72}-BMDMs), or left untreated (Ctrl, *n* = 5 wells). **(B)** mRNA expression of inflammatory mediators in LPS-stimulated WT and *Abca1*$^{-/-}$ mye^{24}-BMDMs (*n* = 6 wells). Dotted line represents untreated BMDMs (Ctrl). **(C)** mRNA expression of inflammatory mediators in LPS-stimulated *Abca1*$^{-/-}$ mye^{24}-BMDMs treated with an SCD1 inhibitor or vehicle (*n* = 5 wells). **(D)** Quantification of FC in *Abca1*$^{-/-}$ mye^{24}-BMDMs treated with a selective SCD1 inhibitor or vehicle (*n* = 4 wells). **(E)** mRNA expression of inflammatory mediators in LPS-stimulated *Abca1*$^{-/-}$ mye^{24}-BMDMs treated with MβCD (2.5% m/v) or vehicle (*n* = 6 wells). **(F–H)** mRNA expression of inflammatory mediators in LPS-stimulated mye^{72}-BMDMs (*n* = 6 wells), -microglia (*n* = 6 wells) and -MDMs (*n* = 4 wells) treated with MβCD or vehicle. Results are pooled from two independent experiments (A–G). Human MDM cultures from four donors were used (H). All data are represented as mean ± SEM. *, P < 0.05, **, P < 0.01, and ***, P < 0.001, unpaired Student's *t* test (A–H).

of phagocytes upon sustained exposure to myelin. Collectively, our findings show that accumulation of FC due to reduced surface ABCA1 abundance underlies the inflammatory phenotype shift of mye-phagocytes.

SCD1 inhibition promotes remyelination in ex vivo organotypic cerebellar brain slices

Remyelination is a regenerative process by which myelin sheaths are restored to demyelinated axons (Franklin and Ffrench-Constant, 2008). Ample evidence indicates that a reduced inflammatory burden favors remyelination (Cantuti-Castelvetri et al., 2018; Karamita et al., 2017; Lan et al., 2018; Makinodan et al., 2016; Vela et al., 2002). Given that SCD1 inhibition and deficiency suppressed the inflammatory status of phagocytes after prolonged myelin incubation, we reasoned that abrogation of SCD1 activity could be a therapeutic target to promote remyelination. Remyelination was first studied using ex vivo cerebellar brain slices demyelinated with lysolecithin (experimental design in Fig. S4 A). In agreement with our in vitro findings, SCD1 inhibition significantly reduced phagocyte cholesterol load and the inflammatory burden in remyelinating cerebellar brain slices (Fig. 8, A–C). Accordingly, F4/80^{+}

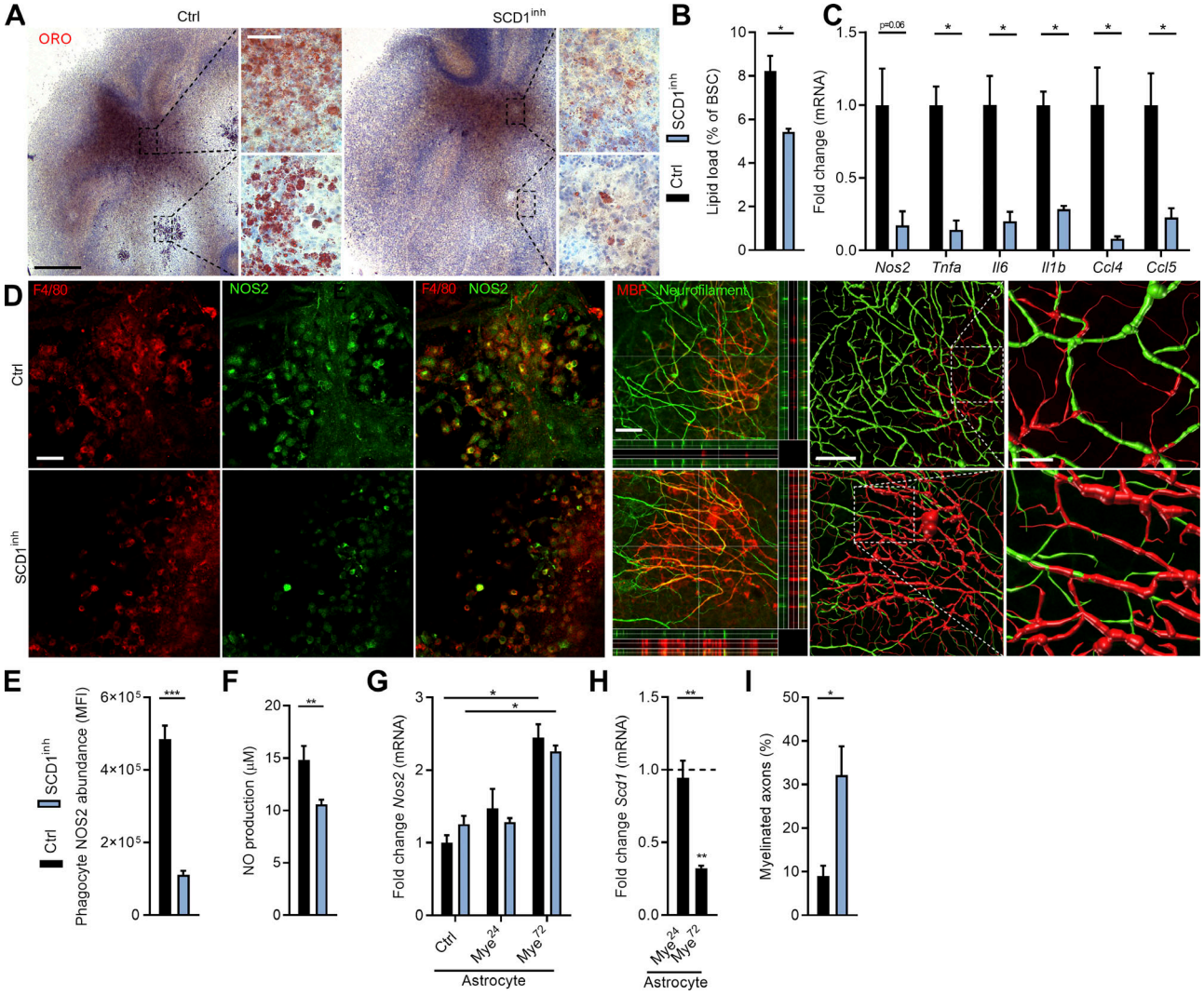

Figure 8. **SCD1 inhibition stimulates remyelination in an ex vivo cerebellar brain slice model. (A and B)** Representative images and quantification (lipid load defined as percent area covered in lipid droplets of the total brain slice area) of ORO (EC) staining of cerebellar brain slices treated with an SCD1 inhibitor or vehicle (n = 3 slices). Scale bars, 500 µm (overview); 50 µm (inset). **(C)** mRNA expression of inflammatory mediators in cerebellar brain slice cultures treated with an SCD1 inhibitor or vehicle (n = 4 slices). **(D)** Representative immunofluorescence images of brain slice cultures treated with vehicle or an SCD1 inhibitor and stained for NOS2/F4/80$^+$ (n = 3 slices; scale bar, 50 µm) and MBP/neurofilament (n = 3 slices; scale bar, 50 µm; orthogonal and three-dimensional reconstruction). **(E)** Quantification of NOS2 abundance (MFI) in F4/80$^+$ phagocytes in brain slices treated with vehicle or an SCD1 inhibitor (n = 3 slices). **(F)** NO concentration in culture supernatants of brain slices treated with an SCD1 inhibitor or vehicle (n = 4 slices). **(G and H)** mRNA expression of *Nos2* and *Scd1* in LPS-stimulated control and myelin-treated (24 h and 72 h) mouse astrocytes cultures (n = 3 wells). Dotted line represents control cultures (H). **(I)** Percentage of MBP$^+$ NF$^+$ axons out of total NF$^+$ axons in brain slices treated with the SCD1 inhibitor or vehicle (n = 4 slices). Results are pooled from or representative of three (A, B, D, E, G, and H) or four (C, F, I, and J) independent experiments. Each replicate represents one brain slice. All data are represented as mean ± SEM. *, P < 0.05, **, P < 0.01, and ***, P < 0.001, unpaired Student's t test (B, C, E, F, H, and I), one-way ANOVA (G).

microglia showed decreased NOS2 immunoreactivity in slices exposed to the SCD1 inhibitor (Fig. 8, D and E), and a reduced concentration of NO was found in the supernatant of these slices (Fig. 8 F). While astrocytes are reported to produce inflammatory mediators such as NO (Liddelow and Barres, 2017), SCD1 inhibition did not change *Nos2* mRNA expression in control and myelin-treated astrocytes in vitro (Fig. 8 G), corresponding to the inability of myelin to increase *Scd1* expression in these cells (Fig. 8 H). In fact, prolonged myelin exposure reduced *Scd1* mRNA expression in astrocytes. Finally, fluorescence staining demonstrated increased colocalization of myelin (myelin basic protein; MBP) and axons (neurofilament) in brain slices treated with the SCD1 inhibitor (Fig. 8, D and I). Three-dimensional reconstruction of these sections confirmed more efficient axonal myelination in slices treated with the SCD1 inhibitor (Fig. 8 D; Peng et al., 2014). These findings show that inhibition of SCD1 promotes myelination of demyelinated axons, and are consistent with the notion that a less inflammatory phagocyte phenotype underlies the repair-promoting effect of SCD1 inhibition.

Phagocyte-specific *Scd1* deficiency stimulates remyelination in vivo

To evaluate the significance of these findings in vivo, the cuprizone-induced de- and remyelination model was induced in

phagocyte-specific *Scd1*$^{-/-}$ mice (experimental design in Fig. S4 B). Cuprizone feeding leads to reproducible toxic demyelination in distinct brain regions such as the corpus callosum (CC). Cessation of cuprizone administration results in spontaneous remyelination. Targeted depletion of *Scd1* in macrophages and microglia was achieved by crossing *Scd1*$^{fl+/+}$ mice with *LysM*$^{Cre+/-}$ mice. SCD1 ablation was validated by immunoblotting (Fig. S4 C). After 6 wk of cuprizone treatment, demyelination was obvious in the CC of both WT and *Scd1*$^{fl+/+}$*LysM*$^{Cre+/-}$ mice, as determined by MBP staining and g-ratio analysis (the ratio of the inner axonal diameter to the total outer diameter; Fig. 9, A–C). 1 wk after termination of cuprizone feeding, *Scd1*$^{fl+/+}$*LysM*$^{Cre+/-}$ mice displayed an increased MBP reactivity and a decreased g-ratio in the CC compared with WT mice, indicating that *Scd1* deficiency in phagocytes promotes remyelination (Fig. 9, A–C). In particular, small diameter axons showed thicker myelin sheaths in *Scd1*$^{fl+/+}$*LysM*$^{Cre+/-}$ mice as compared with control mice (Fig. 9 D). Enhanced remyelination in *Scd1*$^{fl+/+}$*LysM*$^{Cre+/-}$ mice was associated with a reduced inflammatory burden in the CC following demyelination (6 wk) but not during remyelination (6+1 wk; Fig. 9, E and F). The latter finding can be explained by the relative absence of phagocytes in both WT and *Scd1*$^{fl+/+}$*LysM*$^{Cre+/-}$ mice following 1 wk remyelination (Fig. S4, D and E). No differences were observed in the expression of the neurotrophic factors tumor growth factor β (*Tgfb*), ciliary neurotrophic factor (*Cntf*), and insulin growth factor 1 (*Igf1*; Fig. S4, F and G). Interestingly, *Scd1*$^{fl+/+}$*LysM*$^{Cre+/-}$ mice showed decreased cholesterol load in the CC and within phagocytes after demyelination and during remyelination (Fig. 9, G–I). This finding suggests that internalized myelin is more efficiently processed in *Scd1*$^{fl+/+}$*LysM*$^{Cre+/-}$ mice. In support of this notion, *Scd1*$^{fl+/+}$*LysM*$^{Cre+/-}$ mice showed a higher ABCA1 abundance in the CC both after demyelination and during remyelination (Fig. 9, G and J). Importantly, similar effects on remyelination (Fig. S5, A–D), inflammation (Fig. S5, E and F), lipid processing (Fig. S5, G–K), and the expression of neurotrophic factors (Fig. S5, L and M) were observed in whole-body *Scd1*$^{-/-}$ mice. These data show that SCD1 deficiency enhances remyelination by promoting the reparative properties of phagocytes. Collectively, our results identify SCD1 as a novel therapeutic target to promote remyelination.

Discussion

Phagocytes display tremendous diversity and plasticity in vivo, a reflection of dynamic changes in intracellular and extracellular signals (Sica and Mantovani, 2012). Also within MS lesions, divergent phagocyte activation states coexist in close proximity (Boven et al., 2006; Vogel et al., 2013). With respect to mye-phagocytes, some studies reported anti-inflammatory (M2-like) features (Bogie et al., 2011, 2012, 2013; Boven et al., 2006; Kroner et al., 2014; Liu et al., 2006), whereas others reported no effect at all (Glim et al., 2010), or even an inflammatory (M1-like) activation status (Cantuti-Castelvetri et al., 2018; van der Laan et al., 1996; Williams et al., 1994). Our data now indicate that the intracellular myelin load controls the phenotypes that phagocytes display in MS lesions. Sustained internalization of myelin skewed phagocytes toward an inflammatory phenotype that suppressed CNS repair. We further define an intertwined relationship between FA metabolism and this phenotype shift. SCD1, the rate-limiting enzyme in FA desaturation, was found to control the inflammatory phenotype shift of myelin phagocytosing macrophages and microglia by reducing reverse cholesterol transport and promoting the intracellular accumulation of inflammatory cholesterol. Findings from this study explain, at least in part, the progressive nature that MS lesions display and argue for SCD1 inhibition as a promising new therapeutic strategy in MS and other demyelinating diseases.

In demyelinating disorders, foamy phagocytes accumulate a large amount of cytosolic lipid droplets consisting of an inert storage pool of EC (Chang et al., 2006). Based on our findings, we state that esterification of myelin-derived cholesterol, which is predominantly present in its free form in myelin (Saher and Stumpf, 2015), ensues to protect mye-phagocytes from FC-induced toxicity. An increase in SCD1 activity likely provides mye-phagocytes initially with a readily available pool of MUFAs to esterify internalized myelin-derived FC. In this context, palmitoleate and oleate, the end products of SCD1 desaturase activity, make up the bulk of FAs in cholesterol esters (Miyazaki et al., 2000). However, we also found that continuous SCD1 activity skews mye-phagocytes toward an inflammatory phenotype. With time, SCD1-derived MUFAs reduced the capacity of phagocytes to dispose of intracellular cholesterol by decreasing surface ABCA1 abundance in a PKCδ-dependent manner. In line with our findings, previous studies defined that MUFAs can destabilize ABCA1 and inhibit ABCA1-mediated cholesterol efflux (Sun et al., 2003; Wang and Oram, 2002, 2007; Yang et al., 2010). It remains unclear why MUFAs formed by SCD1 are with time no longer used for cholesterol esterification. In particular, our findings indicate that prolonged uptake of myelin by phagocytes markedly increases the cytosolic accumulation of FC. We did not observe alterations in the expression of acyl-CoA: cholesterol acyltransferases or find any morphological indications of ER stress (data not shown), suggesting that inefficient cholesterol esterification or a dysfunctional ER do not underlie the build-up of MUFAs. However, an inability of FC to traffic to the ER and a consequent accumulation of FC in the endosomal and lysosomal compartments may explain the incessant increase in SCD1 activity in myelin overloaded phagocytes. With respect to the latter, aging was recently found to accelerate the accumulation of myelin in phagocytes, which resulted in lysosomal accumulation of FC (Cantuti-Castelvetri et al., 2018). Similar, we observed an increase in the size and number of myelin-containing organelles enclosing unprocessed myelin debris in phagocytes exposed to myelin for a prolonged period of time. Studies focusing on the cellular trafficking and compartmentalization of FC in mye-phagocytes are necessary to certify this hypothesis.

We provide evidence that pharmacological SCD1 inhibition and whole-body or phagocyte-specific *Scd1* deficiency accelerate remyelination. Enhanced remyelination was associated with a decreased cholesterol load and elevated ABCA1 protein levels. These findings strongly suggest that SCD1-induced inhibition of cholesterol efflux suppresses the reparative properties of mye-

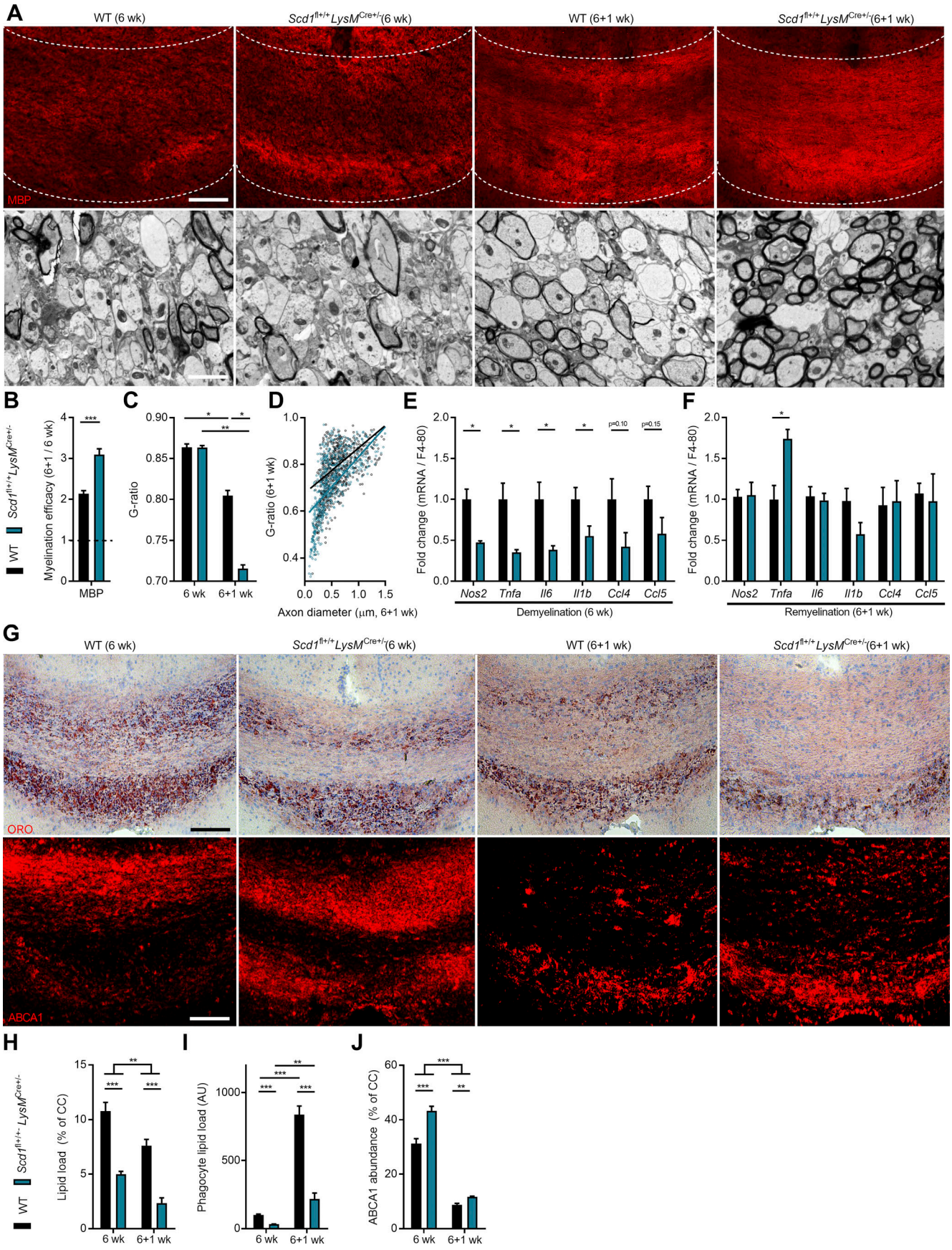
A
WT (6 wk)
Scd1fl+/+LysMCre+/-(6 wk)
WT (6+1 wk)
Scd1fl+/+LysMCre+/-(6+1 wk)
MBP
B
Myelination efficacy (6+1 / 6 wk)
MBP
C
G-ratio
6 wk
6+1 wk
D
G-ratio (6+1 wk)
Axon diameter (µm, 6+1 wk)
E
Fold change (mRNA / F4-80)
Nos2
Tnfa
Il6
Il1b
Ccl4
Ccl5
p=0.10
p=0.15
Demyelination (6 wk)
F
Fold change (mRNA / F4-80)
Remyelination (6+1 wk)
WT
Scd1fl+/+ LysMCre+/-
G
WT (6 wk)
Scd1fl+/+LysMCre+/-(6 wk)
WT (6+1 wk)
Scd1fl+/+LysMCre+/-(6+1 wk)
ORO
ABCA1
H
Lipid load (% of CC)
I
Phagocyte lipid load (AU)
J
ABCA1 abundance (% of CC)

Figure 9. **Phagocyte-specific *Scd1* deficiency improves remyelination in the cuprizone model. (A)** Representative images of immunofluorescence MBP staining and transmission electron microscopy analysis of CC from WT (*Scd1*$^{fl-/-}$*LysM*$^{Cre+/-}$ and *Scd1*$^{fl+/+}$*LysM*$^{Cre-/-}$) and *Scd1*$^{fl+/+}$*LysM*$^{Cre+/-}$ mice after cuprizone-induced demyelination (6 wk) and subsequent remyelination (6+1 wk). The outer border of the CC is demarcated by the dotted line. Scale bars, 100 µm (MBP staining); 2 µm (transmission electron microscopy). **(B)** Quantification of the remyelination efficacy (calculated by dividing the percent myelination at 6+1 wk by the percent myelination at 6 wk using the MBP staining) in CC from WT (6 wk, *n* = 11 animals; 6+1 wk, *n* = 10 animals) and *Scd1*$^{fl+/+}$*LysM*$^{Cre+/-}$ mice (6 wk, *n* = 7 animals; 6+1 wk, *n* = 6 animals). **(C and D)** Analysis of the g-ratio (the ratio of the inner axonal diameter to the total outer diameter) and g-ratio as a function of axon diameter in CC from WT (6 wk, *n* = 4 animals; 6+1 wk, *n* = 8 animals) and *Scd1*$^{fl+/+}$*LysM*$^{Cre+/-}$ mice (6 wk, *n* = 4 animals; 6+1 wk, *n* = 4 animals). **(E and F)** mRNA expression of inflammatory mediators in CC of WT (*n* = 10 or 11 animals, see B) and *Scd1*$^{fl+/+}$*LysM*$^{Cre+/-}$ mice (*n* = 6 or 7 animals, see B) after 6 wk and 6+1 wk. Gene expression was corrected for the number of F4/80$^+$ phagocytes. **(G)** Representative images of ORO (EC) and immunofluorescence ABCA1 staining of CC from WT (*n* = 10 or 11 animals, see B) and *Scd1*$^{fl+/+}$*LysM*$^{Cre+/-}$ (*n* = 6 or 7 animals, see B) mice after 6 wk and 6+1 wk. Scale bar, 100 µm. **(H and I)** Quantification of ORO staining (lipid load defined as percent ORO$^+$ area of total CC area [H] and lipid load corrected for the number of F4/80$^+$ macrophages [I]) and ABCA1 staining (% ABCA1$^+$ area of total CC area) of CC from WT (*n* = 10 or 11 animals, see B) and *Scd1*$^{fl+/+}$*LysM*$^{Cre+/-}$ (*n* = 6 or 7 animals, see B) mice after 6 wk and 6+1 wk. AU, arbitrary unit. All replicates were biologically independent. All data are represented as mean ± SEM. *, P < 0.05, **, P < 0.01, and ***, P < 0.001, unpaired Student's *t* test (B, E, and F), one-way ANOVA (C, H, I, and J).

phagocytes in vivo. In line with our results, defective cholesterol clearance in mye-phagocytes was recently found to limit remyelination in the aged CNS (Cantuti-Castelvetri et al., 2018). Ample evidence indicates that phagocytes drive remyelination by producing neurotrophic factors such as IGF1, TGF-B, and CNTF (Diemel et al., 2004; Kotter et al., 2005; Miron et al., 2013). Here, we did not detect changes in the expression of these mediators in mye-phagocyte cultures and cuprizone animals lacking active SCD1 signaling. However, in all used models enhanced remyelination was closely associated with a reduced expression of inflammatory mediators. Given the inhibitory impact of TNF-A, IL-1B, NO, and IL-6 on remyelination (Cantuti-Castelvetri et al., 2018; Karamita et al., 2017; Lan et al., 2018; Makinodan et al., 2016; Vela et al., 2002), it is tempting to speculate that the reduced inflammatory burden enhanced remyelination in our models. Yet few studies defined that inflammation can also stimulate remyelination by promoting the accumulation, proliferation, and differentiation of oligodendrocyte precursor cells (Arnett et al., 2001; Mason et al., 2001). Thus, while SCD1 inhibition accelerates remyelination and reduces inflammation in our ex vivo and in vivo models, a causal link remains to be determined.

Aside from divergent anatomical niches (Ajami et al., 2011; Mildner et al., 2007), an increasing number of studies indicate that macrophages and microglia differ in their ontogeny, development, and function (Chrast et al., 2011; Goldmann et al., 2016). A comparison of the transcriptomes demonstrated that microglia express a unique cluster of transcripts encoding proteins that sense endogenous ligands (Hickman et al., 2013). In agreement, microglia show an enhanced capacity to internalize myelin as compared with peripheral macrophages (Bogie et al., 2017; Durafourt et al., 2012; Healy et al., 2016). Despite these differences, we show that both phagocyte subsets change their phenotype in a similar fashion upon myelin internalization in vitro. Similar, as *LysM*^{Cre} targets macrophages and microglia (Derecki et al., 2012; Ros-Bernal et al., 2011), enhanced remyelination and reduced inflammation in the CC of *Scd1*$^{fl+/+}$*LysM*$^{Cre+/-}$ likely reflect the impact of SCD1 on both foamy macrophages and microglia in vivo. Further support for involvement of microglia in this process derives from the experiments using the cerebellar brain slice model, which lacks peripheral macrophages altogether. While astrocytes can internalize myelin and display functional divergent phenotypes (Liddelow and Barres, 2017; Ponath et al., 2017), SCD1 inhibition did not affect the inflammatory phenotype of control and myelin-treated astrocytes, nor did prolonged myelin exposure increase *Scd1* expression. The inability of sustained myelin internalization to increase *Scd1* expression in astrocytes merits further investigation. Collectively, our data indicate that SCD1 hampers the reparative of features of foamy phagocytes in demyelinating lesions.

While SFAs are considered to promote the inflammatory status of phagocytes (Anderson et al., 2012; Camell and Smith, 2013), UFAs are mainly known for their anti-inflammatory properties (Camell and Smith, 2013; Souza et al., 2017). Paradoxically, we find that pharmacological and genetic inhibition of *Scd1* alleviates the inflammatory status of mye^{72}-phagocytes, despite decreasing the desaturation index. Through a combination of successive elongation and desaturation reactions, a variety of MUFAs and poly-unsaturated FAs can be formed from SCD1-derived FAs. It remains to be determined which of these UFAs are more pro- or anti-inflammatory in mye-phagocytes. Moreover, the inflammatory outcome of changes in the level of particular UFAs in phagocytes may be context-dependent. For example, ABCA1 destabilization by UFAs is more likely to become inflammatory in phagocytes that rely on lipid efflux to protect themselves from the excessive accumulation of FC, such as the mye-phagocytes described in this study. In support of this notion, ABCA1 deficiency in nonlipid-loaded macrophages induces a pro-angiogenic phenotype, characterized by a reduced expression of inflammatory mediators (Sene et al., 2013). In addition, given that SCD1 deficiency exacerbates inflammation in acute colitis and atherosclerosis models (Chen et al., 2008; MacDonald et al., 2009), changes in particular UFAs may impact inflammation differently in the context of peripheral and myelin-related disorders. More research is warranted to identify culprit UFAs and further unravel the molecular mechanisms that underlie the inflammatory impact of SCD1 on the phenotype of mye-phagocytes.

Remyelination is a complex process that requires an intimate interplay between myelin-forming cells and immunity. Clearance of myelin debris by phagocytes is a critical step in the remyelination process. It not only permits the maturation of oligodendrocyte progenitor cells but also skews phagocytes

toward a reparative phenotype. Here, we show that sustained intracellular accumulation of myelin debris inhibits the reparative features of phagocytes and identifies the SCD1 signaling axis as a crucial driver of this phenotype shift. SCD1 inhibitors are already regarded as promising therapeutics for the treatment of skin disorders, metabolic syndrome, and cancer (Uto, 2016). Our data now indicate that they could also confer therapeutic benefit in demyelinating disorders such as MS.

Materials and methods

Antibodies

The following antibodies were used for immunoblotting: anti-SCD1 (1:1,000, cat. no. 2438S, Cell Signaling Technology), anti-ABCA1 (1:1,000; Lee et al., 2005), and anti-actin (1:5,000, cat. no. sc-47778, Santa Cruz Biotechnology). Appropriate HRP-conjugated secondary antibodies for immunoblotting were purchased from Dako and Cell Signaling Technology. The following antibodies were used for flow cytometry: anti-SCD1 (1:200, cat. no. ab19862, Abcam) and anti-ABCA1 (1:400, cat. no. NB400-105, Novus Biologicals). The following antibodies were used for immunofluorescence: anti-SCD1 (1:250, cat. no. ab19862, Abcam), anti-CCR7 (1:100, cat. no. ab32527, Abcam), anti-CD32 (1:500, cat. no. ab23336, Abcam), anti-IL1B (1:100, cat. no. 12242, Cell Signaling Technology), anti-NOS2 (1:100, cat. no. ab15323, Abcam), anti-NF (1:1,000, cat. no. ab8135, Abcam), anti-IBA1 (1:500, cat. no. 019-19741, Fujifilm), anti-CD68 (1:100, cat. no. 14-0688, Invitrogen), anti-MBP (1:250, cat. no. MAB386, Millipore), anti-F4/80 (1:100, cat. no. MCA497G, Bio-Rad), and anti-ABCA1 (1:200, cat. no. NB400-105, Novus Biologicals). Appropriate secondary antibodies for flow cytometry and immunofluorescence were purchased from Invitrogen.

Mice

Scd1-deficient ($Scd1^{-/-}$) mice and mice having the third exon of the *Scd1* gene flanked by *lox*P sites ($Scd1^{fl+/+}$) are described in previous studies (Miyazaki et al., 2001, 2007). Both mouse strains were backcrossed at least 10 times with C57BL/6J mice. Mice having their 45–46th exon of the *Abca1* gene flanked by *lox*P sites ($Abca1^{fl+/+}$) were kindly provided by J.S. Parks (Department of Pathology/Section on Lipid Sciences, Wake Forest School of Medicine, Winston-Salem, NC; Timmins et al., 2005). This strain was backcrossed to C57BL/6 mice for more than 10 generations. To generate phagocyte-specific $Scd1^{-/-}$ mice, $Scd1^{fl+/+}$ mice were intercrossed with C57BL/6J $LysM^{Cre}$ mice, which were kindly provided by G. van Loo (VIB-UGent Center for Inflammation Research, University of Ghent, Ghent, Belgium; Vereecke et al., 2014). To generate phagocyte-specific $Abca1^{-/-}$ mice, $Abca1^{fl+/+}$ mice were intercrossed with $LysM^{Cre}$ mice. $LXR\alpha^{-/-}$, $LXR\beta^{-/-}$, and $LXR\alpha\beta^{-/-}$ animals on a mixed 129/Sv and C57BL/6J background (backcrossed for at least six generations) are described in previous studies (Alberti et al., 2001; Schuster et al., 2002). All mice were carefully genotyped by PCR as previously described (Alberti et al., 2001; Miyazaki et al., 2007) or according to protocols established by Jackson Laboratories. In all experiments using knockout mice, littermates were used as controls. For experiments using cell-specific knockout mice, $LysM^{Cre+/-}$, $Scd1^{fl+/+}$, and $Abca1^{fl+/+}$ mice were used as controls. For bone marrow isolation, myelin isolation, and brain slice cultures, WT C57BL/6J mice were purchased from Envigo. Mice were maintained on a 12-h light/dark cycle with free access to water and either a standard chow diet or special formulations as indicated. All animal procedures were conducted in accordance with the institutional guidelines and approved by the Ethical Committee for Animal Experiments of Hasselt University.

Myelin isolation and phagocytosis

Myelin was purified from postmortem mouse and human brain tissue by means of density gradient centrifugation, as described previously (Bogie et al., 2017). Myelin protein concentration was determined by using the BCA protein assay kit (Thermo Fisher Scientific), per the manufacturer's guidelines. By using the Chromogenic Limulus Amebocyte Lysate assay kit (Genscript), endotoxin content of isolated myelin was determined to be negligible. To evaluate the ability and extent of myelin phagocytosis, myelin was fluorescently labeled with 1,1′-dioctadecyl-3,3,3′,3′-tetramethylindocarbocyanine perchlorate (DiI; Sigma-Aldrich). Cells were exposed to 100 µg/ml DiI-labeled myelin for 1.5 h and analyzed for fluorescence intensity by using the FACSCalibur (BD Biosciences). To define the uptake of latex beads, cells were exposed to fluorescent red latex beads for 1.5 h (1:100, cat. no. L3030, Sigma-Aldrich).

Macrophage, microglia, and astrocyte differentiation and treatment

Mouse BMDMs and microglia were isolated and differentiated as described previously (Bogie et al., 2017). For astrocytes, mixed glial cells were isolated from pups (postnatal day 0–2). After 2 wk of cultivation, cultures were shaken for 16 h at 250 rpm and 37°C. After the shake-off procedure, the mixed glial cultures were cultured in DMEM medium enriched with 10% FCS and 1% penicillin/streptomycin. Next, astrocytes were purified by differential adhesion and mild trypsinization. BMDMs, microglia, and astrocytes were plated at 0.5×10^6 cells/ml to be used for in vitro experiments. Cells were treated daily with mouse myelin (100 µg/ml) for 24 h (mye^{24}) or 72 h (mye^{72}). To investigate the involvement of downstream pathways, myelin treatment was combined with CAY10566 (SCD1 inhibitor, 1 µM, Cayman Chemicals), Rottlerin (PKCδ inhibitor, 3 µM, Sigma-Aldrich), MβCD (2.5% m/v unless stated otherwise, Sigma-Aldrich), or vehicle treatment for the indicated duration. For inflammatory phenotyping, cells were subsequently stimulated with LPS (100 ng/ml, Sigma-Aldrich) or IFN-G and IL-1B (100 ng/ml, Peprotech) for 6 or 18 h for analysis of gene expression or protein abundance, respectively (Fig. S1 C). To test for SCD1 and ABCA1 ablation, BMDMs were stimulated with T0901317 (10 µM, LXR agonist, Cayman Chemicals) for 24 h before being lysed for immunoblotting.

Human MDMs of healthy controls were isolated as described previously (Bogie et al., 2017). Isolated $CD14^+$ cells were differentiated to macrophages in DMEM supplemented with 10% human serum, 1% penicillin/streptomycin, and 1% L-glutamine. After 6 d, adherent macrophages were harvested and plated at 0.3×10^6 cells/ml to be used for in vitro experiments. MDMs

were treated daily with a dose of human myelin (10 µg/ml) for 24 h (mye^{24}-MDMs) or 72 h (mye^{72}-MDMs), combined with CAY10566 (SCD1 inhibitor, 1 µM) or vehicle treatment. For phenotyping, cells were stimulated with LPS (100 ng/ml) for 6 h or 18 h to assess gene expression or protein level, respectively (Fig. S1 C). All experimental protocols using human cells were conducted in accordance with institutional guidelines and approved by the Medical Ethical Committee of Hasselt University. Written informed consents were obtained from all individual participants included in the study.

Cell line

HeLa-ABCA1^{gfp} expressing GFP-labeled ABCA1 (HeLa-ABCA1^{gfp}; Neufeld et al., 2001) were cultured in DMEM supplemented with 10% FCS and 1% penicillin/streptomycin.

FA treatment

Mouse BMDMs and HeLa-ABCA1^{gfp} cells were treated with 1, 10, or 50 µM of palmitoleic acid (16:1), oleic acid (18:1), 11-eicosenoic acid (20:1), erucic acid (22:1), or nervonic acid (24:1) for 18 h. Next, ABCA1 surface levels and extent of FA uptake were measured using flow cytometry. All FAs were purchased from Sigma-Aldrich.

Immunoblotting

Cells were lysed in radioimmunoprecipitation assay buffer (150 mM NaCl, 50 mM Tris, 1% SDS, 1% Triton X-100, and 0.5% sodium deoxycholate) supplemented with protease-phosphatase inhibitor cocktail (Roche). Samples were separated by electrophoresis on a 7% or 12% gel and were transferred onto a polyvinylidene fluoride membrane. Blots were blocked in 5% milk in Tris-buffered saline, 0.5% Tween 20, and were incubated overnight with relevant primary antibodies at 4°C, followed by incubation with the appropriate HRP-conjugated secondary antibody. An enhanced chemiluminescence plus detection kit (Thermo Fisher Scientific) was used for detection. Densitometry analysis was performed using ImageJ and normalized to actin.

Flow cytometry

Single-cell suspensions were blocked with 10% serum and stained with relevant primary antibodies, followed by incubation with the appropriate secondary antibody. To assess cellular viability, cells were incubated with 7AAD (Thermo Fisher Scientific). The FACSCalibur was used to quantify cellular fluorescence. Mean fluorescence intensity (MFI) was corrected for background MFI.

Nitrite formation and TNF-A production

The release of NO and TNF-A was measured in supernatants from cell cultures using a griess reagent system (Promega) and a commercially available mouse TNF-A ELISA kit (eBioscience), respectively. Both protocols were performed according to the manufacturer's instructions.

Immunofluorescence microscopy and image analysis

Mouse BMDMs and human MDMs were cultured on glass cover slides and fixed in 4% PFA for 20 min. Cerebellar brain slices were fixed in 4% PFA for 40 min. Frozen brain material from active MS lesions was obtained from the Netherlands Brain Bank (Amsterdam, Netherlands). Clinical details of human brain tissue are depicted in Table S1. Cryosections were fixed in acetone for 10 min and in 70% ethanol for 5 min. Immunostaining and analysis of fixed cells and cryosections were performed as described previously (Bogie et al., 2017). To stain cerebellar brain slices, samples were incubated with relevant primary antibody diluted in blocking buffer (1× PBS + 1% BSA + 0.1% Triton X-100). To visualize FC content, fixed cells were incubated with 50 µg/ml Filipin III (Sigma-Aldrich) for 2 h at room temperature. Analysis was performed using a Nikon Eclipse 80i microscope and ImageJ software. The subdivision of the lesion rim and center was accomplished by means of an ORO and proteolipid protein (PLP) staining (rim, ORO$^+$ cells and PLP$^+$ extracellular myelin; center, ORO$^+$ cells and no PLP$^+$ extracellular myelin). Quantification of MFI was performed on original pictures without image enhancement and normalized for background MFI. Three-dimensional analysis of cerebellar brain slices was done using the z-stack function on a LSM880 confocal microscope (Zeiss), followed by three-dimensional rendering using the vaa3d software (Peng et al., 2014). Pictures indicated in figures are digitally enhanced.

ORO staining

To visualize EC, unfixed cryosections and fixed cells were stained with 0.3% ORO (Sigma-Aldrich) for 10 min. Counterstaining of cell nuclei was done using hematoxylin incubation. Analysis was performed using a Leica DM 2000 LED microscope and ImageJ software.

Quantitative PCR

Tissue or cells were lysed using QIAzol (Qiagen). RNA was extracted using the RNeasy mini kit (Qiagen). Complementary DNA was synthesized using the qScript cDNA synthesis kit (Quanta Biosciences) according to the manufacturer's instructions, and quantitative PCR was subsequently conducted on a StepOnePlus detection system (Applied Biosystems). Data were analyzed using the ΔΔCt method and normalized to the most stable reference genes, as described previously (Nelissen et al., 2010; Vandesompele et al., 2002). Primer sequences are available on request.

Cholesterol measurement

Cholesterol efflux by FA-treated BMDMs was defined as described previously (Song et al., 2015). Briefly, cells were exposed to FAs (10 or 50 µM) for 18 h, after which they were labeled with 22-(N-nitrobenz-2-oxa-1,3-diazol-4-yl-amino)-23, 24-bisnor-5-cholen-3-ol (NBD)–cholesterol (Invitrogen) for 4 h. To define ABCA1-mediated efflux, cells were exposed to apoA-I (50 µg/ml; Amar et al., 2010) in phenol- and serum-free medium for 4 h. Intracellular NBD-cholesterol was assessed after cells were lysed with 0.1% Triton X-100 for 30 min. Fluorescence and absorbance were measured using the FLUOstar OPTIMA microplate reader. As myelin interfered with NBD-cholesterol fluorescence, cholesterol efflux by myelin-treated BMDMs was measured by using The Amplex Red Cholesterol Assay Kit. For this purpose,

BMDM and mye-BMDM cultures were exposed to apoA-I (50 µg/ml) in phenol- and serum-free medium for 4 h before measuring intracellular and extracellular total cholesterol. Cholesterol efflux was determined by dividing fluorescence in the supernatants by the total fluorescence in supernatants and cells.

Transmission electron microscopy

Brain samples were fixed with 2% glutaraldehyde. Afterwards, post-fixation was performed with 2% osmiumtetroxide in 0.05 M sodium cacodylate buffer for 1 h at 4°C. Dehydration of the samples was performed by ascending concentrations of aceton. The dehydrated samples were impregnated overnight in a 1:1 mixture of acetone and araldite epoxy resin. Afterwards, the samples were embedded in araldite epoxy resin at 60°C and were cut in slices of 70 nm, perpendicular to the CC, with a Leica EM UC6 microtome and transferred to 0.7% formvar-coated copper grids (Aurion). The samples were contrasted with 0.5% uranyl acetate and lead citrate using a Leica EM AC20. Analysis was performed with a Philips EM208 S electron microscope (Philips) equipped with a Morada Soft Imaging System camera with iTEM-FEI software (Olympus SIS). ImageJ was used to calculate to g-ratio (the ratio of the inner axonal diameter to the total outer diameter), using eight images/animal.

Mass spectrometry imaging (MSI)

Cryosections of active MS lesions were placed on indium tin oxide–coated glass slides (Delta Technologies). Tissue sections were coated with norharmane matrix (Sigma-Aldrich). Matrix was prepared at 7 mg/ml in 2:1 $CHCL_3$:MeOH (vol/vol) and applied to the tissue using a TM-Sprayer (HTX Technologies). MSI was performed using an Orbitrap Elite mass spectrometer (Thermo Fisher Scientific) coupled to an intermediate pressure ion funnel matrix-assisted laser desorption/ionisation (MALDI) source (Spectroglyph LLC; Belov et al., 2017). MSI data were acquired at a pixel size of 40 × 40 μm^2 at a nominal mass resolution of 240,000 (full-width half maximum at m/z 400). MSI images were generated using in house developed software written in MATLAB (MATLAB R2013a; Mathworks). For all data shown, the corresponding $[M+K]^+$ ions of the lipid of interest were used to generate images and were normalized for the total ion current. Mass accuracies were typically within 1 ppm of theoretical m/z values after single point recalibration. Tandem mass spectrometry was performed to determine acyl chain compositions of PC lipid species containing two double bonds in their sum-composition formula. Tandem mass spectrometry was acquired from the corresponding $[M+H]^+$ ions from lesion-containing tissue regions using a mass isolation window of ±0.5 daltons, and higher-energy collisional dissociation.

ESI-MS/MS and GC-MS

Lipid extraction was performed based on a Bligh and Dyer protocol. Briefly, cell pellets were reconstituted in 700 µl PBS, 800 µl CH3OH:HCL(1N) 8:1 (vol/vol), 900 µl $CHCl_3$, and 200 µg/ml of the antioxidant 2,6-di-tert-butyl-4-methylphenol (Sigma-Aldrich). The organic fraction was evaporated using a Speedvac at RT and the remaining lipid pellet was stored under argon at −20°C. Prior to mass spectrometry analysis, lipid pellets were dissolved in running solution (NH4OH:CHCl3:CH3OH; 1.25:10:90; vol/vol/vol). Phospholipids were analyzed by ESI-MS/MS on a hybrid triple quadrupole/linear ion trap mass spectrometer (4000 QTRAP system; SCIEX) equipped with a robotic nanosource for automated sample injection and spraying (TriVersa NanoMate, Advion Biosciences). Phospholipid profiling was executed in positive ion mode by a precursor ion scan (184.1) for PC at a collision energy of 50 eV. Phospholipid quantification was performed in multiple reactions monitoring mode with a signal averaging period of 3 min. Lipid standards PC25:0 and PC43:6 (Avanti Polar Lipids) were added based on the amount of protein in the original sample. Protein concentration was measured using the Pierce BCA Protein Assay Kit (Thermo Fisher Scientific). The data were corrected for hydrogen, nitrogen, carbon, and oxygen isotope effects using the algorithm described by Liebisch et al. (2004). Only lipid species with a signal intensity of at least five times the blank were reported. GC-MS analysis of hydrolyzed FAs derived from BMDM cultures was performed as described previously (Carnielli et al., 1994).

Cuprizone-induced acute demyelination in vivo model

To induce acute demyelination, 9–11-wk-old male mice were fed ad libitum a diet of 0.3% cuprizone (bis[cyclohexanone]oxaldihydrazone, Sigma-Aldrich) mixed in powdered standard chow for 6 wk. The control group consisted of aged-matched male mice that were fed normal chow. Upon withdrawal of the cuprizone diet, spontaneous remyelination occured. After 1 wk of recovery, tissue was collected for histological and biochemical analysis (Fig. S4 B).

Cerebellar slice cultures

Cerebellar slices were obtained from C57BL/6 mouse pups at the age of P9 or P10, as described previously (Hussain et al., 2011; Meffre et al., 2015). To induce demyelination, slices were treated with lysolecithin (0.5 mg/ml; Sigma-Aldrich) for 16 h. After demyelination, slices were treated daily with CAY10566 (SCD1 inhibitor, 10 µM) or vehicle for 1 wk, followed by histological and biochemical analysis (Fig. S4 A).

Statistical analysis

Data were statistically analyzed using GraphPad Prism and are reported as mean ± SEM. The D'Agostino and Pearson omnibus normality test was used to test for normal distribution. When datasets were normally distributed, an ANOVA (Tukey's post hoc analysis) or two-tailed unpaired Student's *t* test (with Welch's correction if necessary) was used to determine statistical significance between groups. If datasets did not pass normality, the Kruskal–Wallis or Mann–Whitney analysis was applied. P values <0.05 were considered to indicate a significant difference (*, $P < 0.05$, **, $P < 0.01$, and ***, $P < 0.001$).

Online supplemental information

Fig. S1 shows changes in SCD1 activity and the inflammatory phenotype of phagocytes upon myelin internalization. Fig. S2 shows functional and morphological changes associated with inhibition of SCD1 in foamy phagocytes. Fig. S3 shows the formation of ABCA1-destablizing FAs upon intracellular accumulation of

myelin. Fig. S4 shows brain pathological parameters in cuprizone-fed *Scd1*$^{fl+/+}$*Lysm*$^{Cre+}$ mice. Fig. S5 shows improved remyelination in whole-body SCD1-deficient mice. Table S1 shows clinical details of human brain tissue used in this manuscript.

Acknowledgments

We thank M.-P. Tulleners and M. Jans for excellent technical assistance. We would also like to thank other members in the Biomedical Research Institute (Hasselt University) for providing feedback and suggestions during preparation of the manuscript.

The work has been supported by the Flemish Fund for Scientific Research (FWO Vlaanderen; 12J9116N, 12JG119N, 12U7718N, and G099618N), the Belgian Charcot Foundation (FCS-2016-EG7, R-8676, and R-6832), the Interreg V-A EMR program (EURLIPIDS, EMR23), and the special research fund UHasselt (BOF). J.-Å. Gustafsson is supported by the Robert A. Welch Foundation (E-0004), the Swedish Cancer Fund, and the Center for Innovative Medicine. N. Zelcer is an Established Investigator of the Dutch Heart Foundation (2013T111) and is supported by a European Research Council Consolidator grant (617376) and by a Netherlands Organization for Scientific Research Vici grant (NWO; 016.176.643). J.M. Ntambi is supported by a National Institutes of Health grant (R01 DK062388).

Author contributions: J.F.J. Bogie, E. Grajchen, N. Zelcer, and J.J.A. Hendriks conceived experiments. J.F.J. Bogie, E. Grajchen, E. Wouters, S. Vanherle, A.G. Corrales, T. Dierckx, M. Haidar, J. Mailleux, P. Gervois, E. Wouters, J. Dehairs, J. Van Broeckhoven, A.P. Bowman, and S.R. Ellis performed experiments. J.F.J. Bogie, E. Grajchen, E. Wouters, S. Vanherle, A.G. Corrales, T. Dierckx, M. Haidar, J. Van Broeckhoven, A.P. Bowman, and S.R. Ellis analyzed data. J.F.J. Bogie, E. Grajchen, E. Wouters, A.G. Corrales, T. Dierckx, M. Haidar, J. Mailleux, J. Van Broeckhoven, A.P. Bowman, J.V. Swinnen, S.R. Ellis, J.M. Ntambi, N. Zelcer, and J.J.A. Hendriks discussed results. P. Gervois, E. Wouters, I. Lambrichts, J.-Å. Gustafsson, A.T. Remaley, M. Mulder, J.V. Swinnen, S.R. Ellis, and J.M. Ntambi, contributed reagents, materials, and analysis tools. J.F.J. Bogie, E. Grajchen, and J.J.A. Hendriks wrote the manuscript. J.F.J. Bogie, E. Grajchen, E. Wouters, A.G. Corrales, T. Dierckx, M. Haidar, P. Gervois, E. Wouters, J. Dehairs, J. Van Broeckhoven, A.P. Bowman, I. Lambrichts, J.-Å. Gustafsson, A.T. Remaley, M. Mulder, J.V. Swinnen, S.R. Ellis, J.M. Ntambi, N. Zelcer, and J.J.A. Hendriks revised the manuscript.

Disclosures: The authors declare no competing interests exist.

Submitted: 5 September 2019
Revised: 12 December 2019
Accepted: 24 January 2020

References

Ajami, B., J.L. Bennett, C. Krieger, K.M. McNagny, and F.M. Rossi. 2011. Infiltrating monocytes trigger EAE progression, but do not contribute to the resident microglia pool. *Nat. Neurosci.* 14:1142–1149. https://doi.org/10.1038/nn.2887

Alberti, S., G. Schuster, P. Parini, D. Feltkamp, U. Diczfalusy, M. Rudling, B. Angelin, I. Björkhem, S. Pettersson, and J.A. Gustafsson. 2001. Hepatic cholesterol metabolism and resistance to dietary cholesterol in LXRbeta-deficient mice. *J. Clin. Invest.* 107:565–573. https://doi.org/10.1172/JCI9794

Amar, M.J., W. D'Souza, S. Turner, S. Demosky, D. Sviridov, J. Stonik, J. Luchoomun, J. Voogt, M. Hellerstein, D. Sviridov, and A.T. Remaley. 2010. 5A apolipoprotein mimetic peptide promotes cholesterol efflux and reduces atherosclerosis in mice. *J. Pharmacol. Exp. Ther.* 334: 634–641. https://doi.org/10.1124/jpet.110.167890

Anderson, E.K., A.A. Hill, and A.H. Hasty. 2012. Stearic acid accumulation in macrophages induces toll-like receptor 4/2-independent inflammation leading to endoplasmic reticulum stress-mediated apoptosis. *Arterioscler. Thromb. Vasc. Biol.* 32:1687–1695. https://doi.org/10.1161/ATVBAHA.112.250142

Arnett, H.A., J. Mason, M. Marino, K. Suzuki, G.K. Matsushima, and J.P. Ting. 2001. TNF alpha promotes proliferation of oligodendrocyte progenitors and remyelination. *Nat. Neurosci.* 4:1116–1122. https://doi.org/10.1038/nn738

Belov, M.E., S.R. Ellis, M. Dilillo, M.R.L. Paine, W.F. Danielson, G.A. Anderson, E.L. de Graaf, G.B. Eijkel, R.M.A. Heeren, and L.A. McDonnell. 2017. Design and Performance of a Novel Interface for Combined Matrix-Assisted Laser Desorption Ionization at Elevated Pressure and Electrospray Ionization with Orbitrap Mass Spectrometry. *Anal. Chem.* 89: 7493–7501. https://doi.org/10.1021/acs.analchem.7b01168

Bogie, J.F., P. Stinissen, N. Hellings, and J.J. Hendriks. 2011. Myelin-phagocytosing macrophages modulate autoreactive T cell proliferation. *J. Neuroinflammation.* 8:85. https://doi.org/10.1186/1742-2094-8-85

Bogie, J.F., S. Timmermans, V.A. Huynh-Thu, A. Irrthum, H.J. Smeets, J.A. Gustafsson, K.R. Steffensen, M. Mulder, P. Stinissen, N. Hellings, and J.J. Hendriks. 2012. Myelin-derived lipids modulate macrophage activity by liver X receptor activation. *PLoS One.* 7:e44998. https://doi.org/10.1371/journal.pone.0044998

Bogie, J.F., W. Jorissen, J. Mailleux, P.G. Nijland, N. Zelcer, T. Vanmierlo, J. Van Horssen, P. Stinissen, N. Hellings, and J.J. Hendriks. 2013. Myelin alters the inflammatory phenotype of macrophages by activating PPARs. *Acta Neuropathol. Commun.* 1:43. https://doi.org/10.1186/2051-5960-1-43

Bogie, J.F., P. Stinissen, and J.J. Hendriks. 2014. Macrophage subsets and microglia in multiple sclerosis. *Acta Neuropathol.* 128:191–213. https://doi.org/10.1007/s00401-014-1310-2

Bogie, J.F., J. Mailleux, E. Wouters, W. Jorissen, E. Grajchen, J. Vanmol, K. Wouters, N. Hellings, J. van Horssen, T. Vanmierlo, and J.J. Hendriks. 2017. Scavenger receptor collectin placenta 1 is a novel receptor involved in the uptake of myelin by phagocytes. *Sci. Rep.* 7:44794. https://doi.org/10.1038/srep44794

Boven, L.A., M. Van Meurs, M. Van Zwam, A. Wierenga-Wolf, R.Q. Hintzen, R.G. Boot, J.M. Aerts, S. Amor, E.E. Nieuwenhuis, and J.D. Laman. 2006. Myelin-laden macrophages are anti-inflammatory, consistent with foam cells in multiple sclerosis. *Brain.* 129:517–526. https://doi.org/10.1093/brain/awh707

Camell, C., and C.W. Smith. 2013. Dietary oleic acid increases m2 macrophages in the mesenteric adipose tissue. *PLoS One.* 8:e75147. https://doi.org/10.1371/journal.pone.0075147

Cantuti-Castelvetri, L., D. Fitzner, M. Bosch-Queralt, M.T. Weil, M. Su, P. Sen, T. Ruhwedel, M. Mitkovski, G. Trendelenburg, D. Lütjohann, et al. 2018. Defective cholesterol clearance limits remyelination in the aged central nervous system. *Science.* 359:684–688. https://doi.org/10.1126/science.aan4183

Carnielli, V.P., E.J. Sulkers, C. Moretti, J.L. Wattimena, J.B. van Goudoever, H.J. Degenhart, F. Zacchello, and P.J. Sauer. 1994. Conversion of octanoic acid into long-chain saturated fatty acids in premature infants fed a formula containing medium-chain triglycerides. *Metabolism.* 43: 1287–1292. https://doi.org/10.1016/0026-0495(94)90224-0

Chang, T.Y., C.C. Chang, N. Ohgami, and Y. Yamauchi. 2006. Cholesterol sensing, trafficking, and esterification. *Annu. Rev. Cell Dev. Biol.* 22: 129–157. https://doi.org/10.1146/annurev.cellbio.22.010305.104656

Chen, C., Y.M. Shah, K. Morimura, K.W. Krausz, M. Miyazaki, T.A. Richardson, E.T. Morgan, J.M. Ntambi, J.R. Idle, and F.J. Gonzalez. 2008. Metabolomics reveals that hepatic stearoyl-CoA desaturase 1 downregulation exacerbates inflammation and acute colitis. *Cell Metab.* 7: 135–147. https://doi.org/10.1016/j.cmet.2007.12.003

Chen, L., J. Ren, L. Yang, Y. Li, J. Fu, Y. Li, Y. Tian, F. Qiu, Z. Liu, and Y. Qiu. 2016. Stearoyl-CoA desaturase-1 mediated cell apoptosis in colorectal cancer by promoting ceramide synthesis. *Sci. Rep.* 6:19665. https://doi.org/10.1038/srep19665

Chrast, R., G. Saher, K.A. Nave, and M.H. Verheijen. 2011. Lipid metabolism in myelinating glial cells: lessons from human inherited disorders and mouse models. *J. Lipid Res.* 52:419–434. https://doi.org/10.1194/jlr.R009761

Chu, K., M. Miyazaki, W.C. Man, and J.M. Ntambi. 2006. Stearoyl-coenzyme A desaturase 1 deficiency protects against hypertriglyceridemia and increases plasma high-density lipoprotein cholesterol induced by liver X receptor activation. *Mol. Cell. Biol.* 26:6786–6798. https://doi.org/10.1128/MCB.00077-06

Derecki, N.C., J.C. Cronk, Z. Lu, E. Xu, S.B. Abbott, P.G. Guyenet, and J. Kipnis. 2012. Wild-type microglia arrest pathology in a mouse model of Rett syndrome. *Nature.* 484:105–109. https://doi.org/10.1038/nature10907

Diemel, L.T., G. Wolswijk, S.J. Jackson, and M.L. Cuzner. 2004. Remyelination of cytokine- or antibody-demyelinated CNS aggregate cultures is inhibited by macrophage supplementation. *Glia.* 45:278–286. https://doi.org/10.1002/glia.10335

Durafourt, B.A., C.S. Moore, D.A. Zammit, T.A. Johnson, F. Zaguia, M.C. Guiot, A. Bar-Or, and J.P. Antel. 2012. Comparison of polarization properties of human adult microglia and blood-derived macrophages. *Glia.* 60:717–727. https://doi.org/10.1002/glia.22298

Flowers, M.T., and J.M. Ntambi. 2008. Role of stearoyl-coenzyme A desaturase in regulating lipid metabolism. *Curr. Opin. Lipidol.* 19:248–256. https://doi.org/10.1097/MOL.0b013e3282f9b54d

Franklin, R.J., and C. Ffrench-Constant. 2008. Remyelination in the CNS: from biology to therapy. *Nat. Rev. Neurosci.* 9:839–855. https://doi.org/10.1038/nrn2480

Glim, J.E., E.J. Vereyken, D.A. Heijnen, J.J. García Vallejo, and C.D. Dijkstra. 2010. The release of cytokines by macrophages is not affected by myelin ingestion. *Glia.* 58:1928–1936. https://doi.org/10.1002/glia.21062

Goldmann, T., P. Wieghofer, M.J. Jordão, F. Prutek, N. Hagemeyer, K. Frenzel, L. Amann, O. Staszewski, K. Kierdorf, M. Krueger, et al. 2016. Origin, fate and dynamics of macrophages at central nervous system interfaces. *Nat. Immunol.* 17:797–805. https://doi.org/10.1038/ni.3423

Grajchen, E., J.J.A. Hendriks, and J.F.J. Bogie. 2018. The physiology of foamy phagocytes in multiple sclerosis. *Acta Neuropathol. Commun.* 6:124. https://doi.org/10.1186/s40478-018-0628-8

Gschwendt, M., H.J. Müller, K. Kielbassa, R. Zang, W. Kittstein, G. Rincke, and F. Marks. 1994. Rottlerin, a novel protein kinase inhibitor. *Biochem. Biophys. Res. Commun.* 199:93–98. https://doi.org/10.1006/bbrc.1994.1199

Healy, L.M., G. Perron, S.Y. Won, M.A. Michell-Robinson, A. Rezk, S.K. Ludwin, C.S. Moore, J.A. Hall, A. Bar-Or, and J.P. Antel. 2016. MerTK Is a Functional Regulator of Myelin Phagocytosis by Human Myeloid Cells. *J. Immunol.* 196:3375–3384. https://doi.org/10.4049/jimmunol.1502562

Hickman, S.E., N.D. Kingery, T.K. Ohsumi, M.L. Borowsky, L.C. Wang, T.K. Means, and J. El Khoury. 2013. The microglial sensome revealed by direct RNA sequencing. *Nat. Neurosci.* 16:1896–1905. https://doi.org/10.1038/nn.3554

Hikawa, N., and T. Takenaka. 1996. Myelin-stimulated macrophages release neurotrophic factors for adult dorsal root ganglion neurons in culture. *Cell. Mol. Neurobiol.* 16:517–528. https://doi.org/10.1007/BF02150231

Hussain, R., M. El-Etr, O. Gaci, J. Rakotomamonjy, W.B. Macklin, N. Kumar, R. Sitruk-Ware, M. Schumacher, and A.M. Ghoumari. 2011. Progesterone and Nestorone facilitate axon remyelination: a role for progesterone receptors. *Endocrinology.* 152:3820–3831. https://doi.org/10.1210/en.2011-1219

Karamita, M., C. Barnum, W. Möbius, M.G. Tansey, D.E. Szymkowski, H. Lassmann, and L. Probert. 2017. Therapeutic inhibition of soluble brain TNF promotes remyelination by increasing myelin phagocytosis by microglia. *JCI Insight.* 2:e87455. https://doi.org/10.1172/jci.insight.87455

Kigerl, K.A., J.C. Gensel, D.P. Ankeny, J.K. Alexander, D.J. Donnelly, and P.G. Popovich. 2009. Identification of two distinct macrophage subsets with divergent effects causing either neurotoxicity or regeneration in the injured mouse spinal cord. *J. Neurosci.* 29:13435–13444. https://doi.org/10.1523/JNEUROSCI.3257-09.2009

Kotter, M.R., C. Zhao, N. van Rooijen, and R.J. Franklin. 2005. Macrophage-depletion induced impairment of experimental CNS remyelination is associated with a reduced oligodendrocyte progenitor cell response and altered growth factor expression. *Neurobiol. Dis.* 18:166–175. https://doi.org/10.1016/j.nbd.2004.09.019

Kroner, A., A.D. Greenhalgh, J.G. Zarruk, R. Passos Dos Santos, M. Gaestel, and S. David. 2014. TNF and increased intracellular iron alter macrophage polarization to a detrimental M1 phenotype in the injured spinal cord. *Neuron.* 83:1098–1116. https://doi.org/10.1016/j.neuron.2014.07.027

Lan, M., X. Tang, J. Zhang, and Z. Yao. 2018. Insights in pathogenesis of multiple sclerosis: nitric oxide may induce mitochondrial dysfunction of oligodendrocytes. *Rev. Neurosci.* 29:39–53. https://doi.org/10.1515/revneuro-2017-0033

Lee, J.Y., J.M. Timmins, A. Mulya, T.L. Smith, Y. Zhu, E.M. Rubin, J.W. Chisholm, P.L. Colvin, and J.S. Parks. 2005. HDLs in apoA-I transgenic Abca1 knockout mice are remodeled normally in plasma but are hypercatabolized by the kidney. *J. Lipid Res.* 46:2233–2245. https://doi.org/10.1194/jlr.M500179-JLR200

Liddelow, S.A., and B.A. Barres. 2017. Reactive Astrocytes: Production, Function, and Therapeutic Potential. *Immunity.* 46:957–967. https://doi.org/10.1016/j.immuni.2017.06.006

Liebisch, G., B. Lieser, J. Rathenberg, W. Drobnik, and G. Schmitz. 2004. High-throughput quantification of phosphatidylcholine and sphingomyelin by electrospray ionization tandem mass spectrometry coupled with isotope correction algorithm. *Biochim. Biophys. Acta.* 1686:108–117. https://doi.org/10.1016/j.bbalip.2004.09.003

Liu, Y., W. Hao, M. Letiembre, S. Walter, M. Kulanga, H. Neumann, and K. Fassbender. 2006. Suppression of microglial inflammatory activity by myelin phagocytosis: role of p47-PHOX-mediated generation of reactive oxygen species. *J. Neurosci.* 26:12904–12913. https://doi.org/10.1523/JNEUROSCI.2531-06.2006

MacDonald, M.L., M. van Eck, R.B. Hildebrand, B.W. Wong, N. Bissada, P. Ruddle, A. Kontush, H. Hussein, M.A. Pouladi, M.J. Chapman, et al. 2009. Despite antiatherogenic metabolic characteristics, SCD1-deficient mice have increased inflammation and atherosclerosis. *Arterioscler. Thromb. Vasc. Biol.* 29:341–347. https://doi.org/10.1161/ATVBAHA.108.181099

Makinodan, M., D. Ikawa, Y. Miyamoto, J. Yamauchi, K. Yamamuro, Y. Yamashita, M. Toritsuka, S. Kimoto, K. Okumura, T. Yamauchi, et al. 2016. Social isolation impairs remyelination in mice through modulation of IL-6. *FASEB J.* 30:4267–4274. https://doi.org/10.1096/fj.201600537R

Mason, J.L., K. Suzuki, D.D. Chaplin, and G.K. Matsushima. 2001. Interleukin-1beta promotes repair of the CNS. *J. Neurosci.* 21:7046–7052. https://doi.org/10.1523/JNEUROSCI.21-18-07046.2001

McMahon, E.J., S.L. Bailey, C.V. Castenada, H. Waldner, and S.D. Miller. 2005. Epitope spreading initiates in the CNS in two mouse models of multiple sclerosis. *Nat. Med.* 11:335–339. https://doi.org/10.1038/nm1202

Meffre, D., C. Massaad, and J. Grenier. 2015. Lithium chloride stimulates PLP and MBP expression in oligodendrocytes via Wnt/β-catenin and Akt/CREB pathways. *Neuroscience.* 284:962–971. https://doi.org/10.1016/j.neuroscience.2014.10.064

Mildner, A., H. Schmidt, M. Nitsche, D. Merkler, U.K. Hanisch, M. Mack, M. Heikenwalder, W. Brück, J. Priller, and M. Prinz. 2007. Microglia in the adult brain arise from Ly-6ChiCCR2+ monocytes only under defined host conditions. *Nat. Neurosci.* 10:1544–1553. https://doi.org/10.1038/nn2015

Mildner, A., M. Mack, H. Schmidt, W. Brück, M. Djukic, M.D. Zabel, A. Hille, J. Priller, and M. Prinz. 2009. CCR2+Ly-6Chi monocytes are crucial for the effector phase of autoimmunity in the central nervous system. *Brain.* 132:2487–2500. https://doi.org/10.1093/brain/awp144

Miron, V.E., A. Boyd, J.W. Zhao, T.J. Yuen, J.M. Ruckh, J.L. Shadrach, P. van Wijngaarden, A.J. Wagers, A. Williams, R.J.M. Franklin, and C. Ffrench-Constant. 2013. M2 microglia and macrophages drive oligodendrocyte differentiation during CNS remyelination. *Nat. Neurosci.* 16:1211–1218. https://doi.org/10.1038/nn.3469

Miyazaki, M., Y.C. Kim, M.P. Gray-Keller, A.D. Attie, and J.M. Ntambi. 2000. The biosynthesis of hepatic cholesterol esters and triglycerides is impaired in mice with a disruption of the gene for stearoyl-CoA desaturase 1. *J. Biol. Chem.* 275:30132–30138. https://doi.org/10.1074/jbc.M005488200

Miyazaki, M., W.C. Man, and J.M. Ntambi. 2001. Targeted disruption of stearoyl-CoA desaturase1 gene in mice causes atrophy of sebaceous and meibomian glands and depletion of wax esters in the eyelid. *J. Nutr.* 131:2260–2268. https://doi.org/10.1093/jn/131.9.2260

Miyazaki, M., M.T. Flowers, H. Sampath, K. Chu, C. Otzelberger, X. Liu, and J.M. Ntambi. 2007. Hepatic stearoyl-CoA desaturase-1 deficiency protects mice from carbohydrate-induced adiposity and hepatic steatosis. *Cell Metab.* 6:484–496. https://doi.org/10.1016/j.cmet.2007.10.014

Nelissen, K., K. Smeets, M. Mulder, J.J. Hendriks, and M. Ameloot. 2010. Selection of reference genes for gene expression studies in rat oligodendrocytes using quantitative real time PCR. *J. Neurosci. Methods.* 187:78–83. https://doi.org/10.1016/j.jneumeth.2009.12.018

Neufeld, E.B., A.T. Remaley, S.J. Demosky, J.A. Stonik, A.M. Cooney, M. Comly, N.K. Dwyer, M. Zhang, J. Blanchette-Mackie, S. Santamarina-Fojo, and H.B. Brewer Jr. 2001. Cellular localization and trafficking of the human ABCA1 transporter. *J. Biol. Chem.* 276:27584–27590. https://doi.org/10.1074/jbc.M103264200

Nikić, I., D. Merkler, C. Sorbara, M. Brinkoetter, M. Kreutzfeldt, F.M. Bareyre, W. Brück, D. Bishop, T. Misgeld, and M. Kerschensteiner. 2011. A reversible form of axon damage in experimental autoimmune encephalomyelitis and multiple sclerosis. *Nat. Med.* 17:495–499. https://doi.org/10.1038/nm.2324

Peng, H., A. Bria, Z. Zhou, G. Iannello, and F. Long. 2014. Extensible visualization and analysis for multidimensional images using Vaa3D. *Nat. Protoc.* 9:193–208. https://doi.org/10.1038/nprot.2014.011

Ponath, G., S. Ramanan, M. Mubarak, W. Housley, S. Lee, F.R. Sahinkaya, A. Vortmeyer, C.S. Raine, and D. Pitt. 2017. Myelin phagocytosis by astrocytes after myelin damage promotes lesion pathology. *Brain.* 140: 399–413. https://doi.org/10.1093/brain/aww298

Ros-Bernal, F., S. Hunot, M.T. Herrero, S. Parnadeau, J.C. Corvol, L. Lu, D. Alvarez-Fischer, M.A. Carrillo-de Sauvage, F. Saurini, C. Coussieu, et al. 2011. Microglial glucocorticoid receptors play a pivotal role in regulating dopaminergic neurodegeneration in parkinsonism. *Proc. Natl. Acad. Sci. USA.* 108:6632–6637. https://doi.org/10.1073/pnas.1017820108

Ruckh, J.M., J.W. Zhao, J.L. Shadrach, P. van Wijngaarden, T.N. Rao, A.J. Wagers, and R.J. Franklin. 2012. Rejuvenation of regeneration in the aging central nervous system. *Cell Stem Cell.* 10:96–103. https://doi.org/10.1016/j.stem.2011.11.019

Saher, G., and S.K. Stumpf. 2015. Cholesterol in myelin biogenesis and hypomyelinating disorders. *Biochim. Biophys. Acta.* 1851:1083–1094. https://doi.org/10.1016/j.bbalip.2015.02.010

Schuster, G.U., P. Parini, L. Wang, S. Alberti, K.R. Steffensen, G.K. Hansson, B. Angelin, and J.A. Gustafsson. 2002. Accumulation of foam cells in liver X receptor-deficient mice. *Circulation.* 106:1147–1153. https://doi.org/10.1161/01.CIR.0000026802.79202.96

Sene, A., A.A. Khan, D. Cox, R.E. Nakamura, A. Santeford, B.M. Kim, R. Sidhu, M.D. Onken, J.W. Harbour, S. Hagbi-Levi, et al. 2013. Impaired cholesterol efflux in senescent macrophages promotes age-related macular degeneration. *Cell Metab.* 17:549–561. https://doi.org/10.1016/j.cmet.2013.03.009

Sica, A., and A. Mantovani. 2012. Macrophage plasticity and polarization: in vivo veritas. *J. Clin. Invest.* 122:787–795. https://doi.org/10.1172/JCI59643

Song, W., W. Wang, Y. Wang, L. Dou, L. Chen, and X. Yan. 2015. Characterization of fluorescent NBD-cholesterol efflux in THP-1-derived macrophages. *Mol. Med. Rep.* 12:5989–5996. https://doi.org/10.3892/mmr.2015.4154

Souza, C.O., A.A. Teixeira, L.A. Biondo, L.S. Silveira, P.C. Calder, and J.C. Rosa Neto. 2017. Palmitoleic acid reduces the inflammation in LPS-stimulated macrophages by inhibition of NFκB, independently of PPARs. *Clin. Exp. Pharmacol. Physiol.* 44:566–575. https://doi.org/10.1111/1440-1681.12736

Sun, Y., M. Hao, Y. Luo, C.P. Liang, D.L. Silver, C. Cheng, F.R. Maxfield, and A.R. Tall. 2003. Stearoyl-CoA desaturase inhibits ATP-binding cassette transporter A1-mediated cholesterol efflux and modulates membrane domain structure. *J. Biol. Chem.* 278:5813–5820. https://doi.org/10.1074/jbc.M208687200

Tall, A.R., and L. Yvan-Charvet. 2015. Cholesterol, inflammation and innate immunity. *Nat. Rev. Immunol.* 15:104–116. https://doi.org/10.1038/nri3793

Timmins, J.M., J.Y. Lee, E. Boudyguina, K.D. Kluckman, L.R. Brunham, A. Mulya, A.K. Gebre, J.M. Coutinho, P.L. Colvin, T.L. Smith, et al. 2005. Targeted inactivation of hepatic Abca1 causes profound hypoalphalipoproteinemia and kidney hypercatabolism of apoA-I. *J. Clin. Invest.* 115:1333–1342. https://doi.org/10.1172/JCI200523915

Trapp, B.D., J. Peterson, R.M. Ransohoff, R. Rudick, S. Mörk, and L. Bö. 1998. Axonal transection in the lesions of multiple sclerosis. *N. Engl. J. Med.* 338:278–285. https://doi.org/10.1056/NEJM199801293380502

Uto, Y. 2016. Recent progress in the discovery and development of stearoyl CoA desaturase inhibitors. *Chem. Phys. Lipids.* 197:3–12. https://doi.org/10.1016/j.chemphyslip.2015.08.018

van der Laan, L.J., S.R. Ruuls, K.S. Weber, I.J. Lodder, E.A. Döpp, and C.D. Dijkstra. 1996. Macrophage phagocytosis of myelin in vitro determined by flow cytometry: phagocytosis is mediated by CR3 and induces production of tumor necrosis factor-alpha and nitric oxide. *J. Neuroimmunol.* 70:145–152. https://doi.org/10.1016/S0165-5728(96)00110-5

Van Raemdonck, K., S. Umar, K. Palasiewicz, S. Volkov, M.V. Volin, S. Arami, H.J. Chang, B. Zanotti, N. Sweiss, and S. Shahrara. 2019. CCL21/CCR7 signaling in macrophages promotes joint inflammation and Th17-mediated osteoclast formation in rheumatoid arthritis. *Cell. Mol. Life Sci.* https://doi.org/10.1007/s00018-019-03235-w

Vandesompele, J., K. De Preter, F. Pattyn, B. Poppe, N. Van Roy, A. De Paepe, and F. Speleman. 2002. Accurate normalization of real-time quantitative RT-PCR data by geometric averaging of multiple internal control genes. *Genome Biol.* 3:H0034. https://doi.org/10.1186/gb-2002-3-7-research0034

Vela, J.M., E. Molina-Holgado, A. Arévalo-Martín, G. Almazán, and C. Guaza. 2002. Interleukin-1 regulates proliferation and differentiation of oligodendrocyte progenitor cells. *Mol. Cell. Neurosci.* 20:489–502. https://doi.org/10.1006/mcne.2002.1127

Vereecke, L., S. Vieira-Silva, T. Billiet, J.H. van Es, C. Mc Guire, K. Slowicka, M. Sze, M. van den Born, G. De Hertogh, H. Clevers, et al. 2014. A20 controls intestinal homeostasis through cell-specific activities. *Nat. Commun.* 5:5103. https://doi.org/10.1038/ncomms6103

Vogel, D.Y., E.J. Vereyken, J.E. Glim, P.D. Heijnen, M. Moeton, P. van der Valk, S. Amor, C.E. Teunissen, J. van Horssen, and C.D. Dijkstra. 2013. Macrophages in inflammatory multiple sclerosis lesions have an intermediate activation status. *J. Neuroinflammation.* 10:35. https://doi.org/10.1186/1742-2094-10-35

Wang, Y., and J.F. Oram. 2002. Unsaturated fatty acids inhibit cholesterol efflux from macrophages by increasing degradation of ATP-binding cassette transporter A1. *J. Biol. Chem.* 277:5692–5697. https://doi.org/10.1074/jbc.M109977200

Wang, Y., and J.F. Oram. 2007. Unsaturated fatty acids phosphorylate and destabilize ABCA1 through a protein kinase C delta pathway. *J. Lipid Res.* 48:1062–1068. https://doi.org/10.1194/jlr.M600437-JLR200

Wang, X., K. Cao, X. Sun, Y. Chen, Z. Duan, L. Sun, L. Guo, P. Bai, D. Sun, J. Fan, et al. 2015. Macrophages in spinal cord injury: phenotypic and functional change from exposure to myelin debris. *Glia.* 63:635–651. https://doi.org/10.1002/glia.22774

Williams, K., E. Ulvestad, A. Waage, J.P. Antel, and J. McLaurin. 1994. Activation of adult human derived microglia by myelin phagocytosis in vitro. *J. Neurosci. Res.* 38:433–443. https://doi.org/10.1002/jnr.490380409

Yamasaki, R., H. Lu, O. Butovsky, N. Ohno, A.M. Rietsch, R. Cialic, P.M. Wu, C.E. Doykan, J. Lin, A.C. Cotleur, et al. 2014. Differential roles of microglia and monocytes in the inflamed central nervous system. *J. Exp. Med.* 211:1533–1549. https://doi.org/10.1084/jem.20132477

Yang, Y., Y. Jiang, Y. Wang, and W. An. 2010. Suppression of ABCA1 by unsaturated fatty acids leads to lipid accumulation in HepG2 cells. *Biochimie.* 92:958–963. https://doi.org/10.1016/j.biochi.2010.04.002

Yvan-Charvet, L., C. Welch, T.A. Pagler, M. Ranalletta, M. Lamkanfi, S. Han, M. Ishibashi, R. Li, N. Wang, and A.R. Tall. 2008. Increased inflammatory gene expression in ABC transporter-deficient macrophages: free cholesterol accumulation, increased signaling via toll-like receptors, and neutrophil infiltration of atherosclerotic lesions. *Circulation.* 118:1837–1847. https://doi.org/10.1161/CIRCULATIONAHA.108.793869

Zhang, X., J. Liu, W. Su, J. Wu, C. Wang, X. Kong, J.A. Gustafsson, J. Ding, X. Ma, and Y. Guan. 2014. Liver X receptor activation increases hepatic fatty acid desaturation by the induction of SCD1 expression through an LXRα-SREBP1c-dependent mechanism. *J. Diabetes.* 6:212–220. https://doi.org/10.1111/1753-0407.12081

Supplemental material

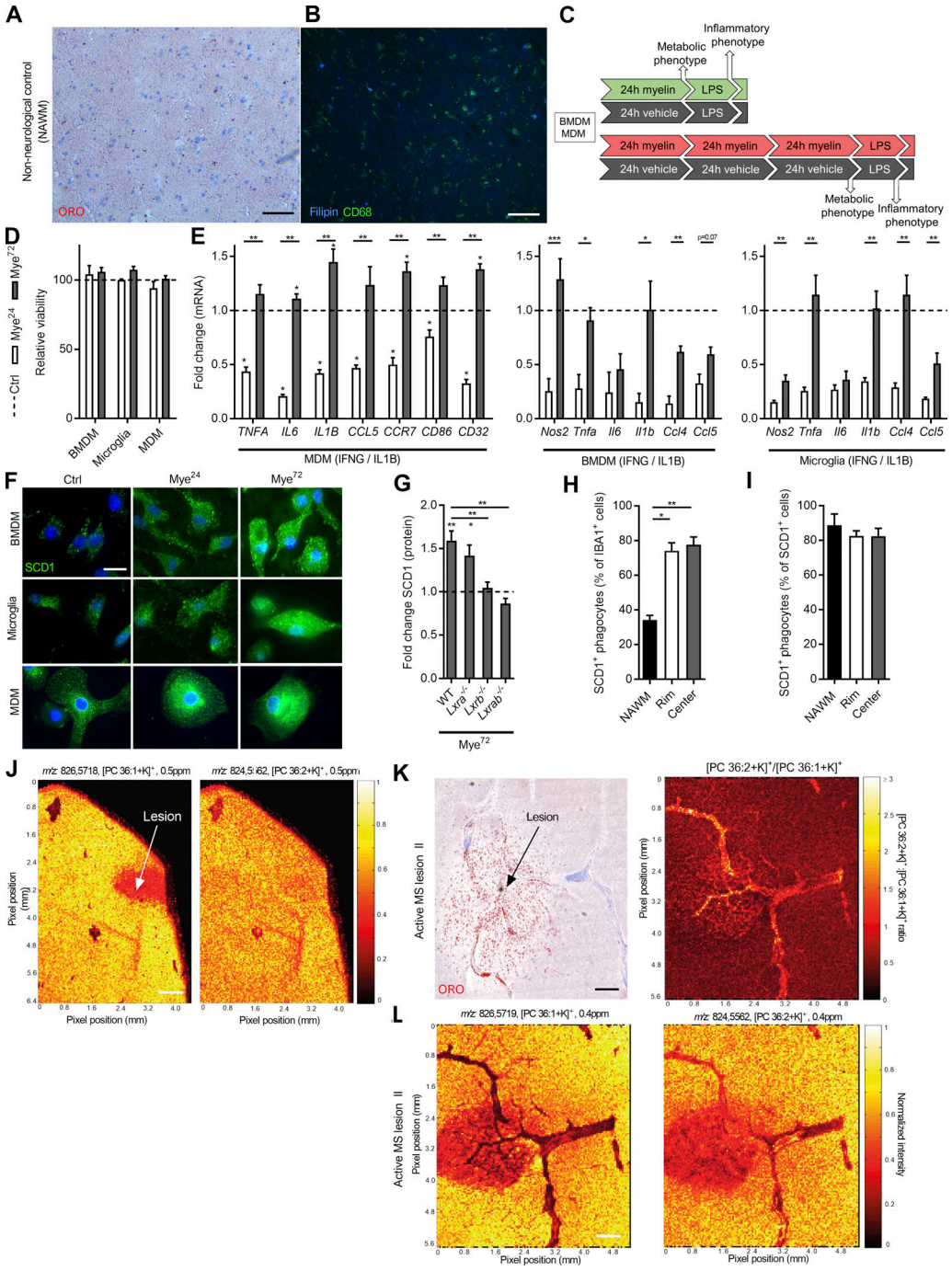

Figure S1. **Sustained exposure to myelin promotes an inflammatory phagocyte phenotype and induces SCD1 abundance and activity. (A and B)** Representative images of ORO (EC) and CD68/filipin (FC) staining of NAWM of control brain tissue (n = 2 nonneurological controls). Scale bar, 100 µm. **(C)** Experimental setup of mouse BMDM, mouse microglia, and human MDM experiments. **(D)** Viability of BMDMs, microglia, and MDMs treated with myelin for 24 or 72 h (n = 4 wells). Dotted line represents untreated cells. **(E)** mRNA expression of inflammatory factors in IFN-G/IL-1B–stimulated BMDMs (n = 5 wells), microglia (n = 6 wells), and MDMs (n = 6 wells) treated with myelin for 24 or 72 h, or left untreated (dotted line, Ctrl). **(F)** Representative images of untreated (Ctrl) and myelin-treated (24 and 72 h) BMDMs, microglia, and MDMs stained for SCD1. **(G)** Flow-cytometric analysis of SCD1 in WT, *LXRα*$^{-/-}$, *LXRβ*$^{-/-}$, and *LXRα*$^{-/-}$*LXRβ*$^{-/-}$ BMDMs treated with myelin for 72 h (n = 5 wells). Dotted line represents untreated BMDMs. **(H and I)** Quantification of the percent of phagocytes expressing SCD1 within the phagocyte pool and the percent of phagocytes expressing SCD1 within the SCD1$^+$ cell pool of active MS lesions stained for SCD1/IBA1 (n = 3 lesions from three different MS patients). **(J)** Representative mass spectrometry images of individual intact PC lipid species (PC36:2 and PC36:1) in active MS lesions (ratio is depicted in Fig. 3 G). Data are represented as normalized intensity. Mass error is depicted in parts per million (ppm). **(K)** Mass spectrometry image of the ratio of intact PC lipid species and corresponding ORO staining of a second active MS lesion. The PC36:2/PC36:1 ratio was calculated based on intensity images of individual PC lipid species. Scale bar, 500 µm. **(L)** Representative mass spectrometry images of PC36:2 and PC36:1 in the second active MS lesion. Data are represented as normalized intensity. Mass error is depicted in parts per million. Results are pooled from or representative of two (A, B, D–F, and J–L) and three (H and I) independent experiments . For human MDM cultures, three (E) and four (D) donors were used. All data are represented as mean ± SEM. *, P < 0.05, **, P < 0.01, and ***, P < 0.001 unpaired Student's t test (A and E), one-way ANOVA (G–I).

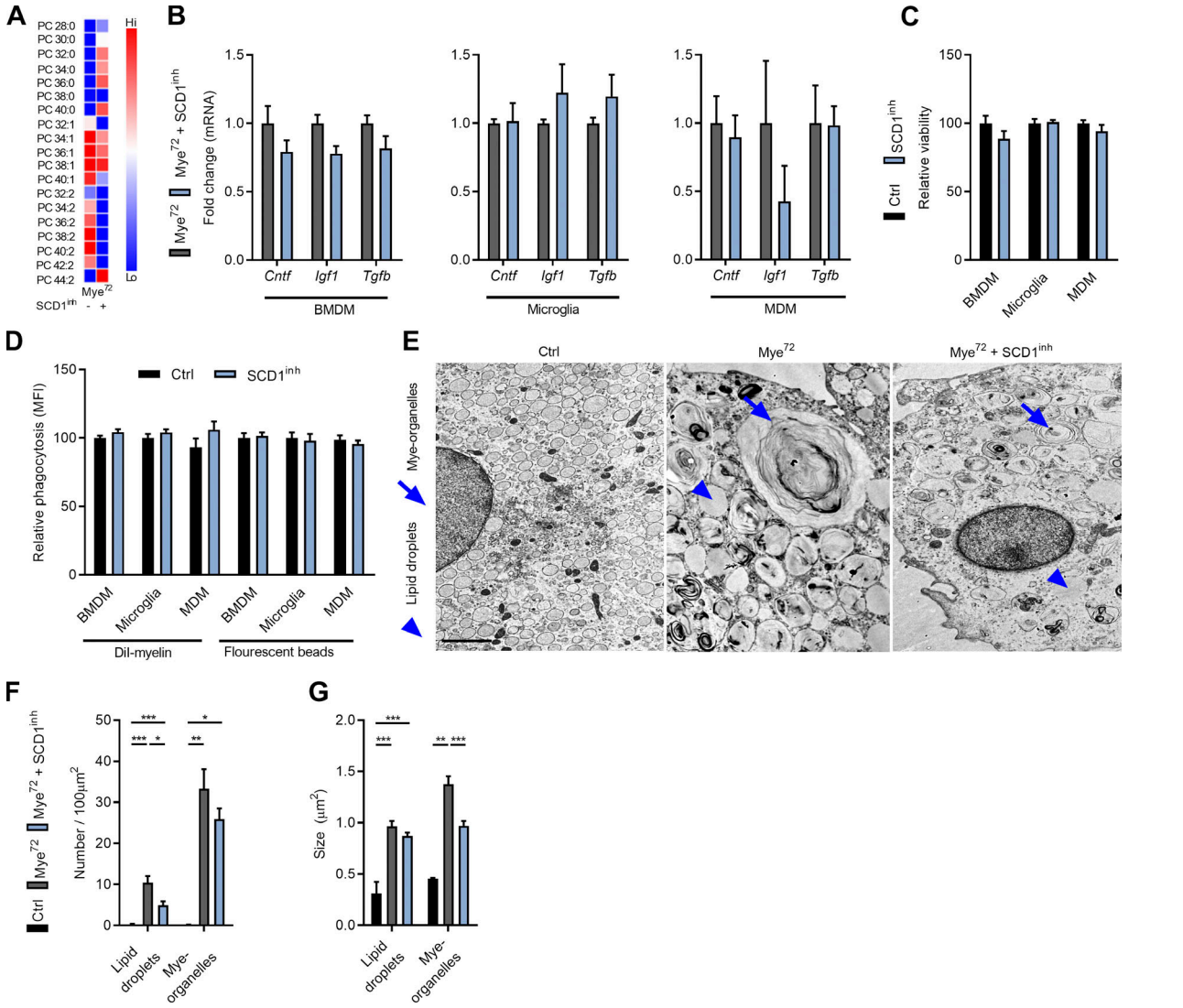

Figure S2. **The impact of SCD1 on the physiology of mye-phagocytes. (A)** ESI-MS/MS–based lipidomics analysis of intact PC in mye^{72}-BMDMs treated with an SCD1 inhibitor or vehicle (n = 2 wells). **(B)** Relative gene expression of neurotrophic factors in LPS-stimulated mye^{72}-BMDMs (n = 5 wells), -microglia (n = 6 wells), and -MDMs (n = 4 wells) treated with an SCD1 inhibitor or vehicle (tumor growth factor β [*Tgfb*], insulin growth factor 1 [*Igf1*], ciliary neurotrophic factor [*Cntf*]). **(C)** Viability of BMDMs (n = 10 wells), microglia (n = 6 wells), and MDMs (n = 8 wells) exposed to an SCD1 inhibitor or vehicle. **(D)** Uptake of fluorescently-labeled myelin (n = 4–6 wells) and beads (n = 4 or 5 wells) by BMDMs, microglia, and MDMs treated with an SCD1 inhibitor or vehicle (Ctrl). **(E)** Representative transmission electron microscopy images of untreated BMDMs (Ctrl), mye^{72}-BMDMs, and mye^{72}-BMDMs treated with an SCD1 inhibitor (n = 4 wells, 5 cells/well were analyzed). Blue arrowheads and arrows point to lipid droplets and myelin-containing organelles (mye-organelles), respectively. Scale bar, 5 µm. **(F and G)** Quantification of the number and size of lipid droplets and mye-organelles in untreated BMDMs (Ctrl), mye^{72}-BMDMs, and mye^{72}-BMDMs treated with an SCD1 inhibitor (n = 4 wells, 5 cells/well were analyzed). Results are pooled from or representative of two (A–G) independent experiments. For human MDM cultures, four donors were used (B–D). All data are represented as mean ± SEM. *, P < 0.05, **, P < 0.01, and ***, P < 0.001, unpaired Student's t test (B–D), one-way ANOVA (F and G).

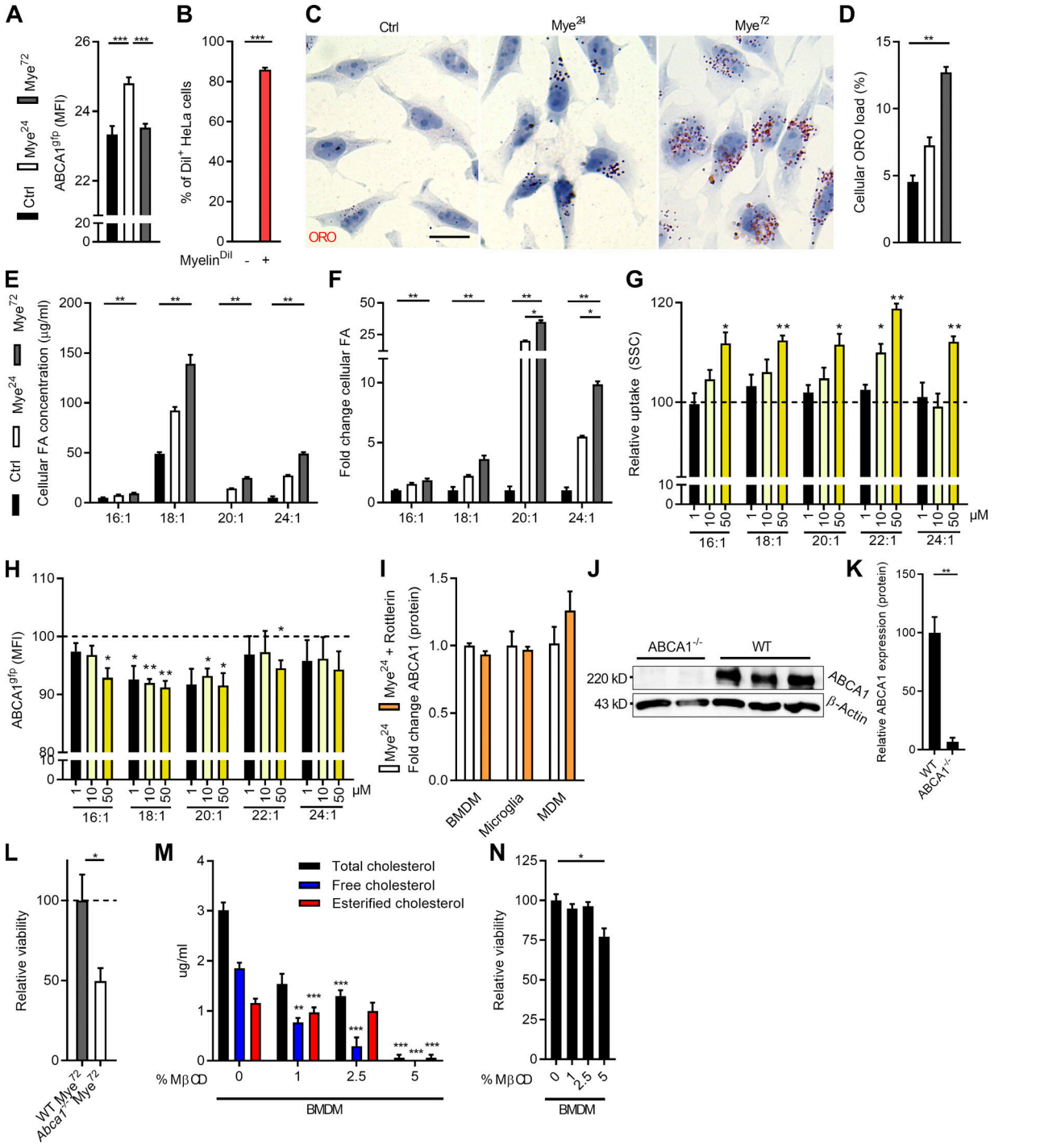

Figure S3. **Sustained myelin internalization increases the formation of ABCA1-destablizing FAs and promotes inflammatory cholesterol accumulation. (A)** ABCA1 abundance in HeLa-ABCA1^{gfp} cells treated with myelin for 24 or 72 h, or left untreated (Ctrl, *n* = 6 wells). **(B)** Uptake of fluorescently labeled myelin (myelin^{DiI}) by HeLa-ABCA1^{gfp} cells (*n* = 4 wells). **(C and D)** Representative images and quantification (percent cell area covered with lipid droplets) of ORO (EC) staining of myelin-treated HeLa-ABCA1^{gfp} cells. Scale bar, 20 µm (*n* = 2 wells). **(E and F)** GC/MS analysis of the methyl esters of FAs hydrolyzed from untreated (Ctrl) and myelin-treated BMDMs (24 or 72 h, *n* = 4 wells). **(G)** Relative uptake of MUFAs (1, 10, and 50 µM), determined by measuring the SSC (*n* = 3 wells). **(H)** ABCA1 abundance in HeLa-ABCA1^{gfp} cells treated with MUFAs for 24 h (1, 10, and 50 µM; *n* = 4 wells). **(I)** Surface ABCA1 abundance on myelin-treated (24 h) mouse BMDMs (*n* = 5 wells), mouse microglia (*n* = 6 wells), and human MDMs (*n* = 4 wells) exposed to rottlerin (PKCδ inhibitor) or vehicle. **(J and K)** Immunoblot analysis of ABCA1 protein levels in WT and *Abca1*$^{fl+/+}$*Lysm*$^{Cre+/-}$ BMDMs stimulated with the LXR agonist T0901317 (*n* = 2/3 cultures of different animals). **(L)** Viability of WT and *Abca1*$^{-/-}$-BMDMs exposed to myelin for 72 h (*n* = 4 wells). **(M and N)** Cholesterol content (*n* = 7 wells) and viability (*n* = 7 wells) of mye^{72}-BMDMs exposed to MβCD (1, 2.5, and 5% m/v) or vehicle. Results are pooled from or representative of two (A–J, M, and N) and three (K and L) independent experiments. For human MDM cultures, four donors were used (I). All data are represented as mean ± SEM. *, P < 0.05, **, P < 0.01, and ***, P < 0.001, one-way ANOVA (A, D–H, M, and N), unpaired Student's *t* test (B, K, and L).

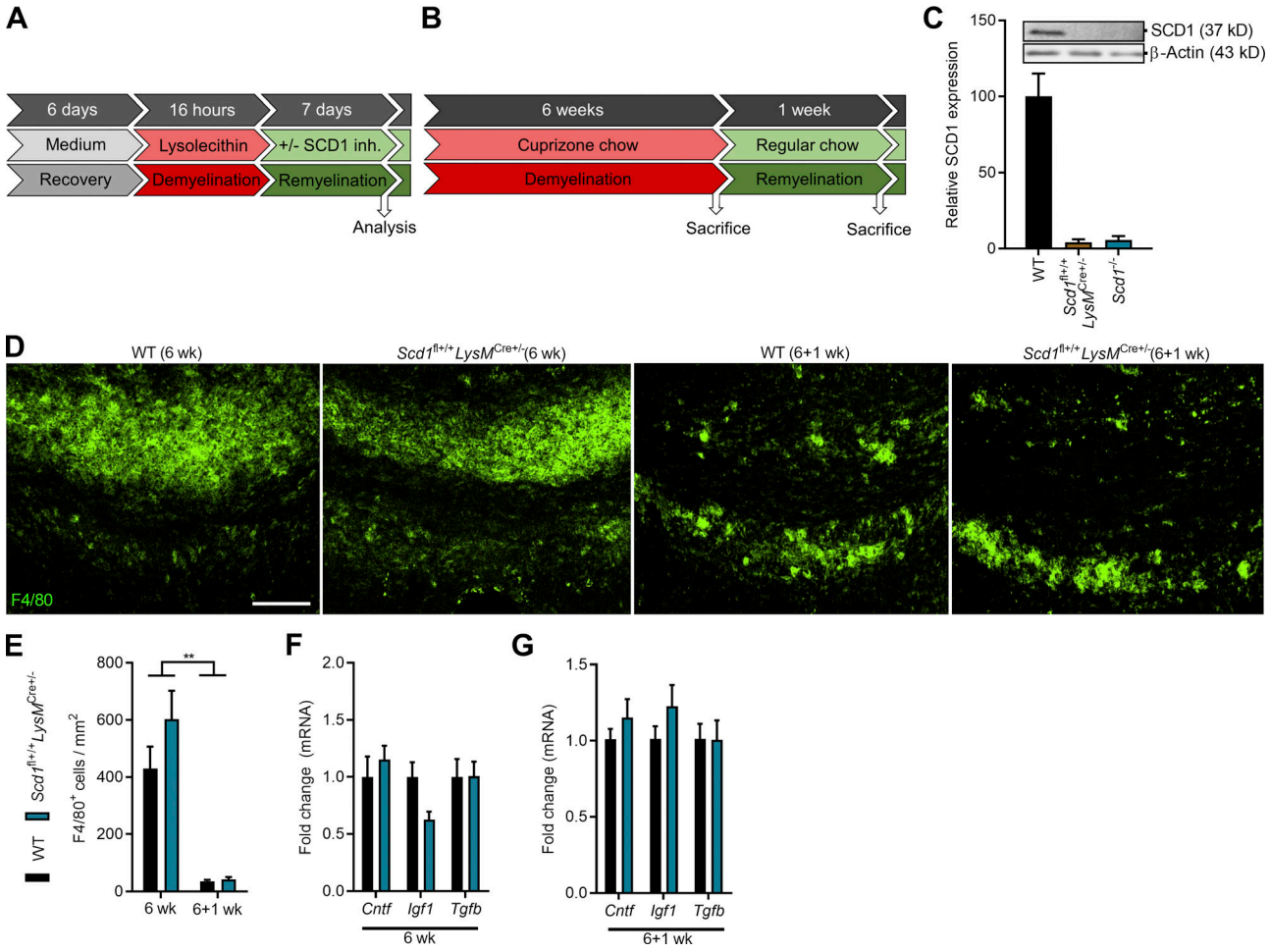

Figure S4. **Confirmation of SCD1 ablation and pathological parameters of *Scd1*$^{fl+/+}$*Lysm*$^{Cre+}$ mice. (A and B)** Experimental setup of the brain slice culture model for remyelination (A) and cuprizone-induced acute demyelination in vivo model (B). SCD1 inh., SCD1 inhibitor. **(C)** Immunoblot analysis of SCD1 protein in WT, *Scd1*$^{fl+/+}$*Lysm*$^{Cre+/-}$, and *Scd1*$^{-/-}$ BMDMs stimulated with the LXR agonist T0901317 (n = 2 cultures of different animals). **(D and E)** Representative immunofluorescence images and quantification of F4/80 staining of CC from WT (6 wk, n = 11 animals; 6+1 wk, n = 10 animals) and *Scd1*$^{fl+/+}$*LysM*$^{Cre+/-}$ mice (6 wk, n = 7 animals; 6+1 wk, n = 6 animals). Scale bar, 100 µm. **(F and G)** mRNA expression of neurotrophic factors in CC of WT (6 w, n = 11 animals; 6+1 wk, n = 10 animals) and *Scd1*$^{fl+/+}$*LysM*$^{Cre+/-}$ mice (6 w, n = 7 animals; 6+1 wk, n = 6 animals) after cuprizone-induced demyelination (6 w) and subsequent remyelination (6+1 wk). All replicates were biologically independent. All data are represented as mean ± SEM. **, P < 0.01, unpaired Student's t test (E–G).

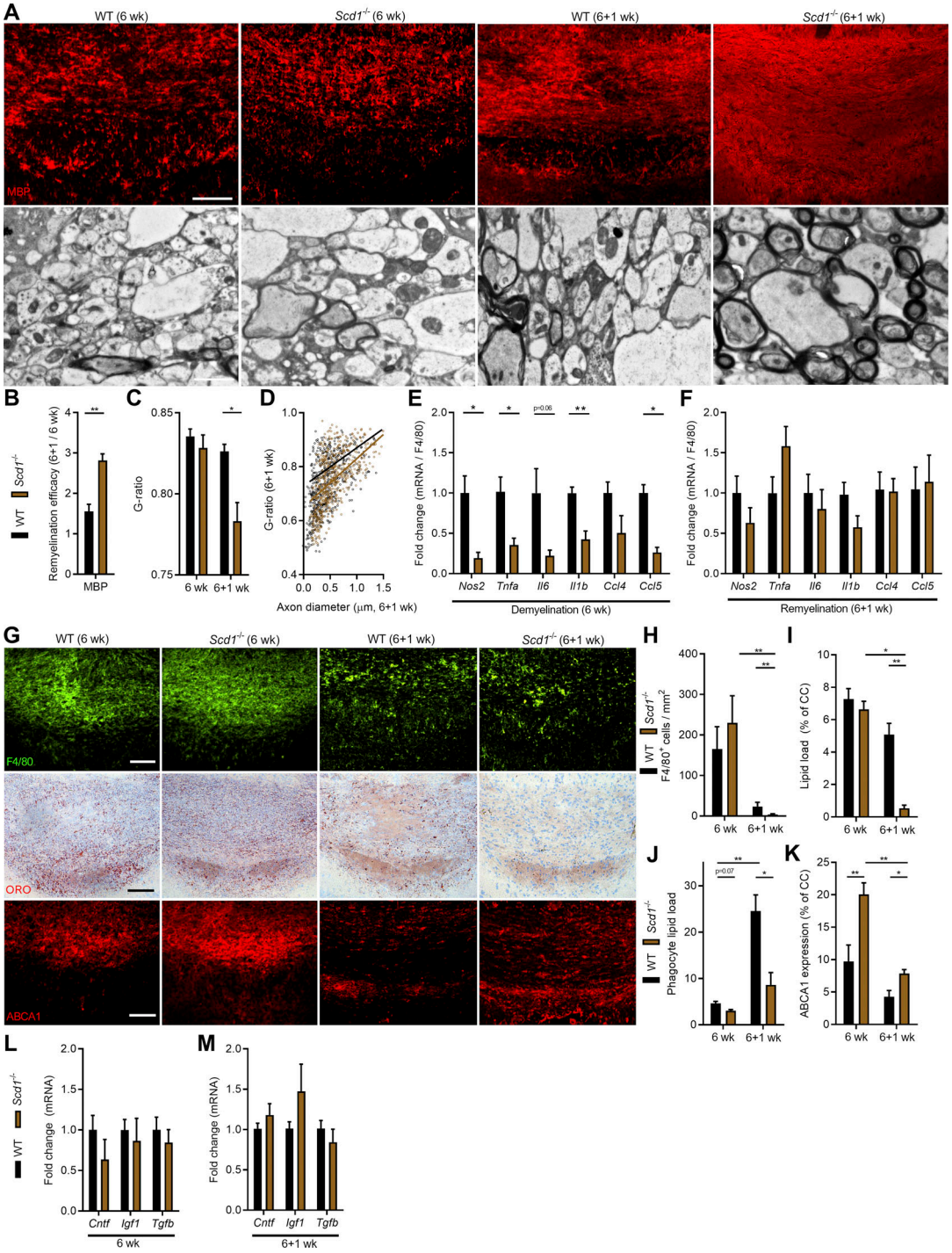

Figure S5. **Whole-body *Scd1* deficiency improves remyelination in the cuprizone model. (A)** Representative images of immunofluorescence MBP staining and TEM analysis of CC derived from WT and *Scd1*$^{-/-}$ mice after cuprizone-induced demyelination (6 wk) and subsequent remyelination (6+1 wk; *n* = 5 animals/group). Scale bars, 100 µm (MBP staining); 2 µm (TEM). **(B)** Quantification of the remyelination efficacy (calculated by dividing the percent myelination at 6+1 wk by the percent myelination at 6 wk using the MBP staining) in CC from WT and *Scd1*$^{-/-}$ mice (*n* = 5 animals/group). **(C and D)** Analysis of the g-ratio (the ratio of the inner axonal diameter to the total outer diameter) and g-ratios as a function of axon diameter in CC from WT (6 wk, *n* = 4 animals; 6+1 wk, *n* = 2 animals) and *Scd1*$^{-/-}$ mice (6 wk, *n* = 4 animals; 6+1 wk, *n* = 2 animals). **(E and F)** mRNA expression inflammatory mediators in CC of WT and *Scd1*$^{-/-}$ mice after 6 wk (*n* = 5 animals) and 6+1 wk (*n* = 9 animals). Gene expression was corrected for the number of F4/80^{+} phagocytes. **(G)** Representative images of F4/80, ORO (EC), and ABCA1 staining of CC from WT and *Scd1*$^{-/-}$ mice after cuprizone-induced demyelination (6 wk, *n* = 5 animals/group) and subsequent remyelination (6+1 wk, *n* = 5 animals/group). Scale bar, 100 µm. **(H–K)** Quantification of F4/80 staining, ORO staining (lipid load defined as percent ORO^{+} area of total CC area, lipid load corrected for number of F4/80^{+} macrophages), and ABCA1 staining (% ABCA1^{+} area of total CC area; *n* = 5 animals/group). **(L and M)** mRNA expression of neurotrophic factors in CC of WT and *Scd1*$^{-/-}$ mice after cuprizone-induced demyelination (6 wk, *n* = 5 animals/group) and subsequent remyelination (6+1 wk, *n* = 9 animals/group). All replicates were biologically independent. All data are represented as mean ± SEM. *, P < 0.05, and **, P < 0.01, unpaired Student's *t* test (B, E, F, L, and M), one-way ANOVA (C and H–K).

Table S1 is provided online as a separate Word document and lists clinical details of human brain tissue.